# Dual-Band, Two-Layer Millimeter-Wave Transceiver for Hybrid MIMO Systems

Susnata Mondal, *Member, IEEE*, Larry Richard Carley, *Life Fellow, IEEE*, and Jeyanandh Paramesh, *Senior Member, IEEE*

***Abstract*— This article presents a two-layer low-complexity fully connected (FC) RF/analog weighting multi-input–multi-output (MIMO) transceiver comprising an RF weight layer and an analog–baseband weight layer. The transceiver can serve as a small-scale MIMO system by itself and can serve as the building block in a larger hybrid MIMO system. The architecture mitigates the complexity versus spectral-efficiency tradeoffs of existing MIMO architectures and enables MIMO stream/user scalability, superior energy efficiency, and spatial-processing flexibility. A compact, reconfigurable bidirectional circuit architecture is introduced, including a new Cartesian-combining/splitting beamforming receiver/transmitter, dual-band bidirectional beamforming network, dual-band frequency translation chains, and baseband Cartesian beamforming with an improved programmable gain amplifier design. A 28-/37-GHz band, two-layer, eight-element, four-stream hybrid MIMO transceiver prototype is designed in 65-nm CMOS to demonstrate the above features. The prototype achieves accurate beam/null-steering capability, excellent area/power efficiency, and state-of-the-art TX/RX mode performance in two simultaneous bands while demonstrating multi-antenna (up to eight) multi-stream (up to four) over-the-air spatial multiplexing operation using the proposed energy-efficient two-layer hybrid beamforming scheme.**

***Index Terms*— Carrier aggregation, digital beamforming, fifth generation (5G), full-duplex, fully connected (FC), hybrid beamforming (HBF), millimeter-wave transceiver, multi-input–multi-output (MIMO), phased array.**

## I. Introduction

MULTI-INPUT–MULTI-OUTPUT (MIMO) communication based on millimeter-wave beamforming is expected to play a central role in beyond-fifth-generation (5G) wireless systems. In the quest for higher data rates and channel capacity, systems are being developed based on a wide variety of architectures [1]–[10]. Digital beamforming-based (DBF) MIMO architectures having per-element frequency translation and analog–digital interfaces are attractive from the standpoint of flexibility and performance but can be expensive in terms of cost and energy efficiency [11]–[13]. Hybrid beamforming (HBF)-based MIMO architectures offer a pathway to implementing MIMO with lower cost and with performance approaching that of DBFs. Two kinds of HBF architectures are being pursued in the algorithmic [14]–[23] and circuit communities [10], [24], [25], namely, the partially connected (PC) and fully connected (FC) type. FC HBFs have been shown to have superior performance over PC HBFs [16], [22]–[26], but scaling FC-HBFs to higher stream count has posed serious challenges in terms of complexity and power consumption.

This article introduces a transceiver that can function as a small-scale MIMO system by itself [27]. The transceiver can be also tiled for use in a larger MIMO system. Within the transceiver, a low-complexity FC topology is effectively formed between $P$ antennas and $Q$ baseband inputs/outputs using a combination of an RF weighting layer and an analog baseband weighting layer. The transceiver includes $Q$ upconversion and $Q$ downconversion chains, henceforth referred to as RF chains. The RF weighting layer adopts an FC topology, which: 1) enables better spectral efficiency compared to a PC topology due to a higher number of degrees of freedom [16], [22], [26]; 2) offers support for carrier aggregation using the full antenna aperture [24]; and 3) facilitates full-duplex beamforming with per-element self-interference cancellation (SIC) [25], [27].

This article also describes circuit architecture and circuit designs that can lead to a compact, low-cost implementation. A "Cartesian-splitting" transmit beamforming architecture is introduced, which is merged with the Cartesian-combining receive beamforming architecture [10], [24], [28]. The transceiver, which is designed for dual-band operation, features a bidirectional beamforming network with extensive passive structure reuse, up/downconversion chains, LO generation and distribution, Cartesian weights for baseband beamforming, and a phase-invariant programmable gain amplifier design. A 28-/37-GHz eight-element, four-stream transceiver prototype is designed and characterized to demonstrate the proposed systemic, architectural, and circuit concepts. The chip also incorporates on-chip digital engines for autonomous array pattern adaptation and for SIC in full-duplex mode. Note that, in the full-duplex mode, individual antennas are only used for transmit or receive (with SIC) at any instant in time, but the array is both transmitting and receiving. These topics and associated on-air measurements were reported briefly in [27] but are not within the scope of this article.

Manuscript received February 17, 2021; revised June 6, 2021 and August 14, 2021; accepted August 23, 2021. This article was approved by Associate Editor Pietro Andreani. This work was supported in part by the National Science Foundation under Grant CRI-1823235. *(Corresponding author: Susnata Mondal.)*

The authors are with the Department of Electrical and Computer Engineering, Carnegie Mellon University, Pittsburgh, PA 15213 USA (e-mail: susnatam@alumni.cmu.edu).

Color versions of one or more figures in this article are available at https://doi.org/10.1109/JSSC.2021.3110520.

Digital Object Identifier 10.1109/JSSC.2021.3110520

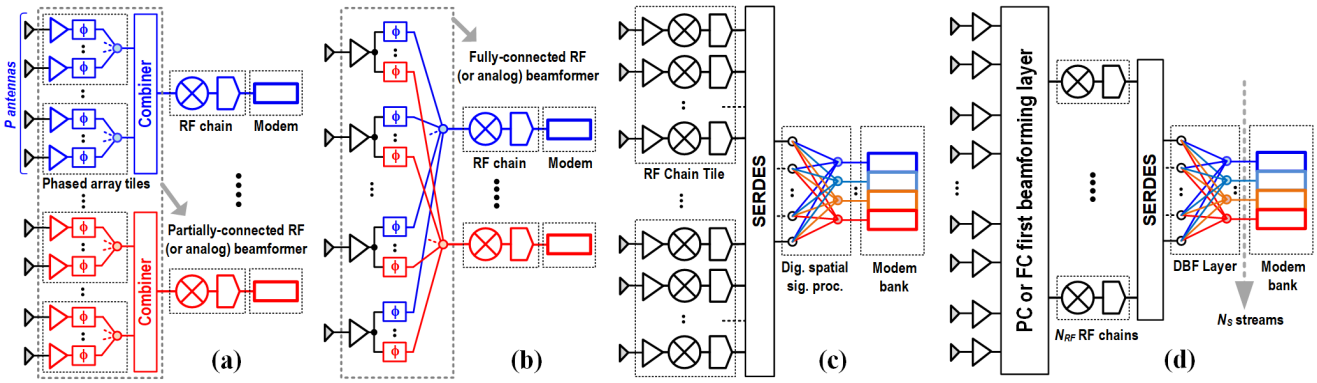


Fig. 1. MIMO system architectures: (a) single-layer MIMO using phased (PC) sub-array beamforming, (b) single-layer MIMO using FC RF beamforming, (c) single-layer MIMO using per-element digital beamforming, and (d) two-layer MIMO architecture (HBF).

## II. Multi-Layer MIMO Architectures

### A. Single-Layer MIMO Architectures

Fig. 1(a)–(c) illustrates three single-layer MIMO receiver architectures. Dual approaches can be devised for MIMO transmitters. The architecture of Fig. 1(a) uses conventional phased array tiles organized into sub-arrays. Each tile applies RF beamforming weights to a group of $P$ antennas and combines the outputs into one stream. In order to scale up the total number of antennas ($N_A$), outputs from several tiles can be combined at RF and then downconverted, digitized, and demodulated. A $P$-element sub-array in Fig. 1(a) is associated with a single data stream. In order to scale up the number of user streams ($N_S$), several sub-arrays can be replicated, one per stream. This approach is simple and modular and is based on mature phased array technology. Moreover, in a receiver, each sub-array spatially filters all-but-one streams and other interferers before downconversion, which can ease the dynamic range requirements of the RF chains and data converters. However, for the fixed aperture area, only a subset of antenna elements in the aperture is available to each stream. Moreover, the cross-stream isolation entirely depends on the spatial filtering of the RF beamformer. This results in reduced beamforming gain per stream with increasing $N_S$ and reduced spatial filtering of blockers prior to each RF chain.

A second MIMO architecture is based on an FC beamformer [see Fig. 1(b)]. Here, each RF chain accesses every element in the antenna array aperture via an independently programmable complex-weight, achieving better per-stream beamforming gain and spatial filtering. This is an important advantage over the sub-array architecture. Mondal *et al.* [10] and Mondal and Paramesh [24] demonstrated FC tiles with eight and four elements, respectively, and two RF chains. While it is feasible to increase the number of antennas, scaling up the number of RF chains (and, thus, $N_S$) is significantly more challenging due to RF/analog circuit and routing complexity. Therefore, a "flat" FC architecture is impractical for large $N_S$.

A third single-layer MIMO architecture [see Fig. 1(c)] is based on DBF using *per-element* RF chains and I/Q A/D conversion. DBF offers complete flexibility, scalability, and the best spectral efficiency since advanced beamforming techniques, such as true time-delay, per-subcarrier, or frequency-domain weighting, can be easily implemented. Moreover, since the RF, analog–baseband, and analog–digital interfaces in DBFs are modular, DBFs can, in principle, be easily scaled to large $N_A$, given the availability of a sufficiently capable DSP. However, DBFs can be expensive in terms of power and die area in large antenna arrays in the RF, analog, and digital portions, as well as the local data link (SerDes) layer [11], [13]. Moreover, in DBF receivers, since no spatial filtering occurs before digitization, the dynamic range and the effective number of bits in the ADCs are increased when the desired streams are accompanied by unwanted co-channel interferers.

### B. Two-Layer MIMO Architectures

Another possible approach to scaling $N_A$ and $N_S$ is to augment a first RF/analog beamforming layer with a second beamforming layer at baseband (typically digital, but can also be analog), as shown in Fig. 1(d). This results in the so-called HBF MIMO architecture (one layer at RF and one layer at baseband) [14], [15], [23], [26]. The first layer can have a PC topology [e.g., Fig. 1(a), gray dashed box] or an FC topology [similar to the gray dashed box in Fig. 1(b)]. In HBFs, the number of RF chains and A/D interfaces scales with $N_S$, rather than $N_A$ as in the case for DBFs.

Mathematically, both PC and FC HBFs essentially seek to factorize the equivalent DBF beamforming matrix into a product of RF and baseband beamforming matrices. Numerous systems articles [14]–[23] report mathematical techniques to perform such factorization under various constraints. Most of these papers adopt a "flat" $N_A \times N_S$ FC RF layer, which we noted becomes impractical for sufficiently large $N_A$ and $N_S$. On the other hand, a two-layer HBF MIMO using a PC first layer has fewer degrees of freedom than the FC-based HBF, which can lead to a significant performance penalty compared to DBF [16], [22], [26].

### C. System Simulation Example

In Section II-D, we describe an architecture to mitigate the aforementioned shortcomings. Presently, to gain an intuitive

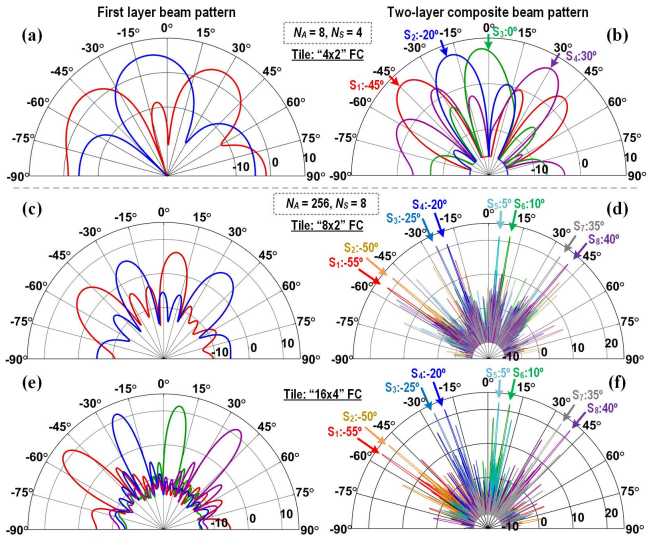


Fig. 2. System simulation illustrating two-layer beamforming. Design example for $N_A = 8$, $N_S = 4$, and $4 \times 2$ FC tile: (a) first layer only and (b) two-layer overall beam pattern. Design example for $N_A = 256$, $N_S = 8$, and $8 \times 2$ FC tile: (c) first layer only and (d) two-layer overall beam pattern. Design example for $N_A = 256$, $N_S = 8$, and $16 \times 4$ FC tile: (e) first layer only and (f) two-layer overall beam pattern.

understanding of HBF operation and motivate the architecture, we consider two system simulations: a small-scale hybrid MIMO system (called S1) with $N_A = 8$ and $N_S = 4$, and a large-scale hybrid MIMO system (called S2) with $N_A = 256$ and $N_S = 8$. For S2, two cases are considered: the first having 32 "$8 \times 2$" tiles (a tile with $P$ antennas and $Q$ downconversion chains is referred to as "$P \times Q$" tile) and the second having 16 "$16 \times 4$" tiles, in the RF beamforming first layer. In all cases, the first layer is followed by a second layer implemented in digital.

In S1, the input streams $S_1$–$S_4$ [see Fig. 2(b)] are assumed to arrive at well-separated angles. In S2, the input streams $S_1$–$S_8$ [see Fig. 2(d) and (f)] are grouped into four pairs that arrive at well-separated angles, but the two streams within each pair have small angular separation so that they cannot be resolved by the first beamforming layer. All streams are assumed to have equal power at the antennas, and no interferers are present. Fig. 2(a), (c), and (e) shows the beam patterns formed by a single tile in the first layer, with a distinct color being used to represent the beam pattern at a particular output of the tile. Fig. 2(b), (d), and (f), which shows the array patterns after beamforming by both layers, reveals that, in all cases, narrow beams (whose beamwidths depend on $N_A$ in each system) are formed that simultaneously provide per-stream beamforming gain and cross-stream isolation. For S1, in Fig. 2(a), one output from a $4 \times 2$ tile captures $S_1$ and $S_4$ by forming a beam having two "main" lobes (shown in red); the other output captures $S_2$ and $S_3$ by forming a beam having a single main lobe (shown in blue). For S2, with $8 \times 2$ first-layer tiles, each output captures four streams by forming a beam having two "main" lobes [see Fig. 2(c)]. For S2, with $16 \times 4$ tiles, each output captures two streams [see Fig. 2(e)] by forming a beam with a single main lobe.

Thus, in all cases, the first layer provides a part of the overall beamforming gain and partial cross-stream isolation due to spatial filtering (i.e., each beam isolates and partially rejects two streams in S1, four streams S2/8 $\times$ 2, and six streams in S2/16 $\times$ 4). The remaining cross-stream isolation and the beamforming gain are provided by the second beamforming layer. It should be noted that co-channel (and other close-in) interferers will be suppressed by spatial filtering in the first layer, which will reduce dynamic range requirements on downstream circuits.

HBF in transmit arrays can be understood similarly. Each tile sends out signals simultaneously in many different directions for many streams. The input to each tile (upconverted from baseband) is already pre-processed in such a way that each stream after the cumulative effect of all tiles constructively adds in only one of many transmit directions.

In previous work [10], [24], we demonstrated $4 \times 2$ and $8 \times 2$ FC tiles having only RF-domain weights. Prior experience from [10] and [24] and circuit-level simulations indicates that it is feasible to increase the number of antennas supported by a tile (perhaps to 16 or 32), but increasing the number of RF chains in an FC tile using only RF weights is difficult. For example, implementing the $16 \times 4$ tile described above may be impractical using RF weights only. Therefore, we propose a low-complexity FC tile architecture that uses a combination of RF weights to perform the first layer of beamforming and analog baseband weights to perform the second layer of beamforming. Note that, in this way, additional spatial filtering of the signal at the ADC input will further reduce the requirements on the data converters relative to the case where the second layer combining is done in the digital domain.

### *D. Proposed Low-Complexity FC Tile Architecture*

The proposed tile is shown in Fig. 3 (dashed blue box) in receive-path configuration in the context of a larger hybrid MIMO system. A tile comprises $L$ groups of $P/L \times Q/L$ independent RF-domain complex-weights. Each $P/L \times Q/L$ RF weight group is topologically FC, which means that independent weights can be applied between the $P/L$ antennas and the RF ports of $Q/L$ RF chains. It should be noted that each tile can be trivially configured in PC topology simply by turning off several RF weights. At the baseband ports of the $Q$ RF chains, $(Q \times Q)$ analog complex-weights are applied. The analog weights have an FC topology. Together, the RF and analog weights form a low-complexity FC first layer between $P$ antennas and $Q$ baseband nodes in the sense that any input can be connected to any output. However, the total number of degrees of freedom in this HBF structure is lower than in an RF-only FC structure. Thus, the proposed low-complexity FC topology offers a range of tradeoffs between implementation complexity and accessible degrees of freedom. By itself, the transceiver tile can operate as a small-scale hybrid MIMO system; indeed, all measurement results shown later in this article were conducted at this level. Also, a larger MIMO system can be constructed using $K = N_A/P$ such tiles, which can be interfaced with data converters, SerDes, and the digital back end, as shown in Fig. 3.

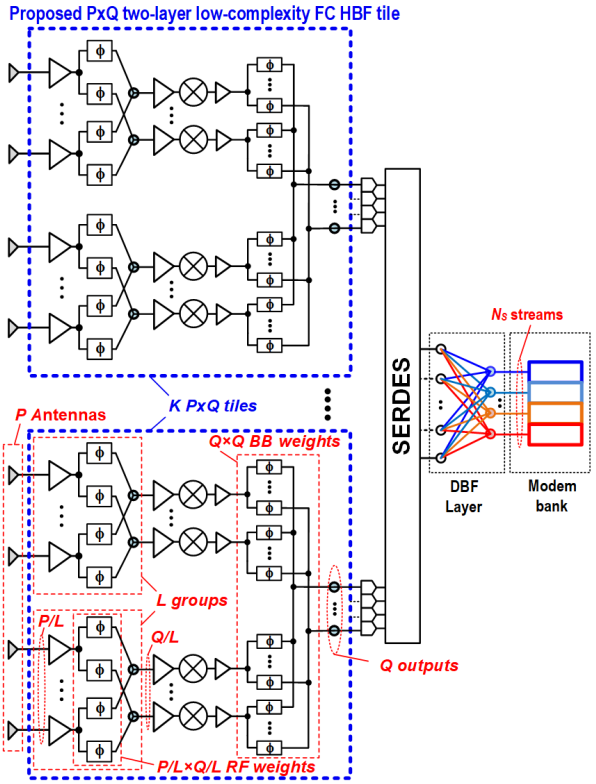


Fig. 3. Proposed two-layer transceiver tile (dashed blue box) embedded in a hybrid MIMO system.

Key benefits of the proposed low-complexity FC tile are summarized next. *First*, as noted previously, it offers a higher number of degrees of freedom in an HBF compared to a PC-based tile [16], [22], [26]. *Second*, independent beams can be formed at different carrier frequencies (within the passband regions of the frequency response of the signal path) since the paths from each antenna from/to each RF chain's I/O have independently programmable complex-weights. Thus, the architecture supports a form of multi-antenna carrier aggregation, where each carrier can achieve the entire beamforming gain available from the aperture [24], regardless of whether the tile has two layers or a single layer. Note that such carrier aggregation where each carrier is aggregated from all antennas cannot be performed in an HBF based on PC tiles. *Third*, the low-complexity FC tile inherently supports a per-element SIC mechanism to cancel TX leakage in a simultaneous transmit–receive system. Design details of this SIC mechanism, as well as initial characterization results of full-duplex communication for single and multiple antenna cases, were provided in [25] and [27]. Further details in this mode will be the scope of a future publication. It should be noted that the PC tile- and FC tile-based architectures have an equal number of LNA/PA stages, frequency translation chains, corresponding LO circuitry, and A/Ds for identical $P$ and $Q$. However, a two-stream FC tile has twice the complexity in the RF beamforming layer. Sections III and IV describe architectural and circuit techniques that make the beamforming layer design power and area efficient, thereby minimizing the overhead.

## III. Transceiver Architecture

The RF weighting layer is implemented using the Cartesian-combining/splitting technique in the receive/transmit paths, respectively. The analog–baseband weighting layer is implemented using transconductor-based PGAs in conjunction with current-combining.

### A. Cartesian-Splitting MIMO/Beamforming Transmit Path

Although the Cartesian-combining principle has been used extensively in receivers, the dual of this approach for transmitters seems to have not been reported. Therefore, the "Cartesian-splitting" architecture for beamforming transmitters is developed in this section. We begin by referring to Fig. 4(a), which shows a quadrature upconverter followed by a vector modulator complex-weighting circuit and a power amplifier driving an antenna element. Our immediate goal is to eliminate the quadrature splitter (typically implemented as a quadrature hybrid or polyphase filter) from the signal path. This can be done by two transformations: first, by commutating the RF splitting and the quadrature upconversion operations [see Fig. 4(b)]; and second, by absorbing the 90° phase shifter in the RF signal path into the LO ports of the mixers and appropriately modifying the connections of the LO phases [see Fig. 4(c)]. The Cartesian-splitting complex-weighting principle can also be understood mathematically. The complex baseband signal, $\tilde{x}_{BB}(t) \equiv x_{BBI}(t) + jx_{BBQ}(t)$, is upconverted by a complex quadrature mixer, producing a complex-valued signal with *real* and *imaginary* parts $u_r(t)$ and $u_i(t)$

$$u(t) = \tilde{x}_{BB}(t)e^{j2\pi f_{LO}t} \doteq u_r(t) + ju_i(t)$$

where

$$\begin{aligned} u_r(t) &= x_{BBI}(t)C - x_{BBQ}(t)S, u_i(t) = x_{BBI}(t)S + x_{BBQ}(t)C \\ C &\equiv \cos(2\pi f_{LO}t), \quad S \equiv \sin(2\pi f_{LO}t). \end{aligned} \tag{1}$$

In a phased array or PC MIMO transmitter, each antenna must be driven by an independent complex-weighted signal. Thus, the signal driving the $k$th antenna (or the $k$th PA) can be generated by independently gain-scaling the *real* and *imaginary* parts and summing them together, as shown in (2a)

$$\begin{aligned} x_k(t) &\overset{(a)}{=} A_r u_r(t) - A_i u_i(t) = \mathrm{Re}[(A_r + jA_i)u(t)] \\ &\overset{(b)}{=} \mathrm{Re}\left[(A_r + jA_i)\tilde{x}_{BB}(t)e^{j2\pi f_{LO}t}\right] \\ &= A_r\left\{x_{BBI}(t)C - x_{BBQ}(t)S\right\} - A_i\left\{x_{BBI}(t)S + x_{BBQ}(t)C\right\}. \end{aligned} \tag{2}$$

Equivalently, (2b) shows that the envelope of the bandpass signal $x_k(t)$ is equal to the complex baseband envelope scaled by a complex-valued weight $(A_r + jA_i)$. In practice, gain scaling of the *real* and *imaginary* parts can be implemented by a pair of programmable gain transconductors, while the summing can be implemented by combining their output currents.

It is straightforward to extend the aforementioned principle to an FC hybrid MIMO transmitter. As shown in Fig. 4(d) for a single antenna in a two-stream FC-MIMO transmitter,

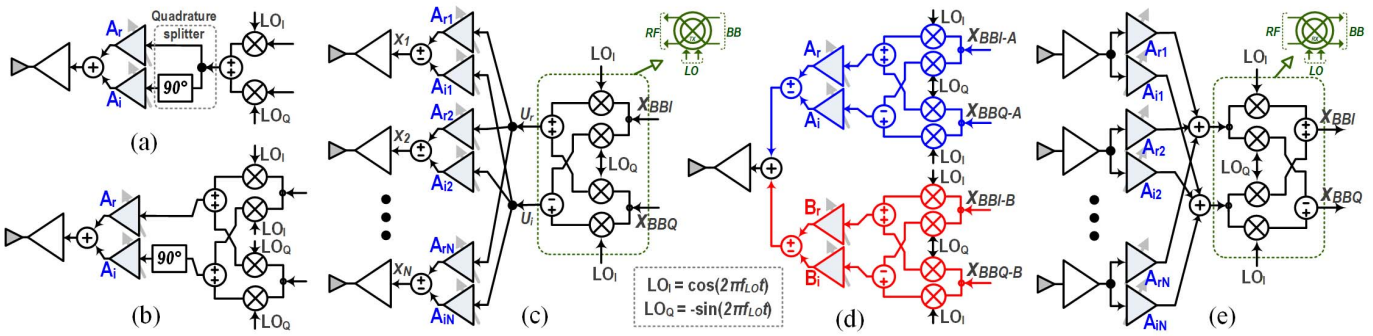


Fig. 4. (a) Vector-modulator-based Cartesian phase-shifting single-element transmitter. (b) Modified vector modulator architecture—RF splitting inside the quadrature splitter is translated to baseband. (c) Cartesian-splitting-based beamforming transmitter architecture—90° phase shifter is absorbed in the LO path from RF. (d) Cartesian-splitting-based phase shifting for one element and two baseband streams—one stream shown in blue and the other in red. (e) Cartesian-combining-based receiver beamforming architecture shown for single-stream reception.

a separate upconversion chain is required for each stream. In order to apply a complex-weight for the $s$th stream to the $k$th antenna, the *real* and *imaginary* outputs of the $s$th chain are scaled with a pair of PGAs $A_{r;k,s}$ and $A_{i;k,s}$. The weighted streams are then summed together before the $k$th antenna. In our transmitter, summing is done at the input of the $k$th PA; this signal can be written as

$$x_k(t) = \mathrm{Re}\left[\sum_{s=1}^{S}\{A_{r;k,s} + jA_{i;k,s}\}\tilde{x}_{BB,s}(t)e^{j2\pi f_{LO}t}\right]. \quad (3)$$

### *B. Cartesian-Combining MIMO/Beamforming Receive Path*

The Cartesian-combining architecture was originally proposed in [28] for single-stream RF beamforming with homodyne down-conversion [see Fig. 4(e)]. It was extended to hybrid MIMO reception in [10], which also introduced a heterodyne embodiment having image filtering, but no image cancellation. In [24], a generalized heterodyne embodiment with reconfigurable image cancellation was introduced to support sole or concurrent dual-band reception. By using a single LO generation circuit in each downconversion chain, Mondal and Paramesh [24] supported MIMO reception at either 28 GHz or 37 GHz, or concurrently in both bands. In this work, the receive signal path is designed to support both the 28- and 37-GHz bands, either solely or concurrently. In contrast to [24], a direct conversion approach is adopted here; this necessitates a dedicated LO distribution circuit for each downconversion chain but obviates the need for image-reject calibration [24]. Note that the direct conversion approach additionally requires LO leakage reduction, especially for the transmit path.

### *C. Advantages of Cartesian Combining/Splitting Technique*

In this work, the Cartesian-combining receive path and the Cartesian-splitting transmit path are combined to implement a bidirectional MIMO transceiver, which is shown schematically in Fig. 5 (detailed schematics of various sub-circuits are shown later in this article, as indicated at the bottom of Fig. 5). This circuit architecture has several advantages. First, it avoids the use of RF-domain phase shifters or quadrature hybrids that are typically lossy, bulky, and narrowband and typically have single-ended signal paths with low-Q matching interfaces. Second, using the circuit design techniques described in [10], high resolution, calibration-free, digitally programmable Cartesian complex-weighting with low gain and phase error can be implemented. Third, and most importantly, the weighting principle is inherently wideband and is applicable at any frequency where the front-end PGAs can achieve sufficient gain. Therefore, this architecture is well suited for wideband applications and also for dual-band applications over widely separated frequencies. Note that, in a Cartesian beamforming transceiver, since the baseband circuitry and the frequency conversion chain are shared between all antenna elements, the additional circuitry required in the front end compared to a single antenna transceiver is a single pair of PGAs. It should be noted that overhead of the Cartesian architecture is its need for a pair of combining/splitting paths for each receive/transmit stream. However, since this architecture avoids some of the mm-wave passive blocks in the front end that are typically large, the front end can be ultra-compact, which, in turn, helps shorten mm-wave routing. Furthermore, by shortening mm-wave routing, active current mode combiners can be used with low loss resulting in two advantages. First, active combiners can be designed to operate in widely separated frequency bands; second, they can enable reconfigurability between TX, RX, and full-duplex mode (see Section IV-B for more details).

## IV. Transceiver Circuit Design

A 28-/37-GHz two-layer HBF MIMO transceiver tile with eight elements and four chains has been designed to demonstrate the concepts described previously. The prototype follows Fig. 3 with parameter values $P = 8$, $L = 2$, and $Q = 4$. A block diagram is shown in Fig. 5. The RF weight layer comprises two four-element FC groups (also referred to as FC-tiles, hereafter). In each group, the antenna port is interfaced with two RF chains via front-end amplifiers and PGAs for complex-weighting. Thus, the prototype has four complete upconversion and downconversion RF chains that are implemented in an inter-leaved manner, as shown in Fig. 5.[1]

[1]The inter-leaving approach was taken to facilitate one of the three SIC mechanisms for STAR operation, which was described briefly in [27].

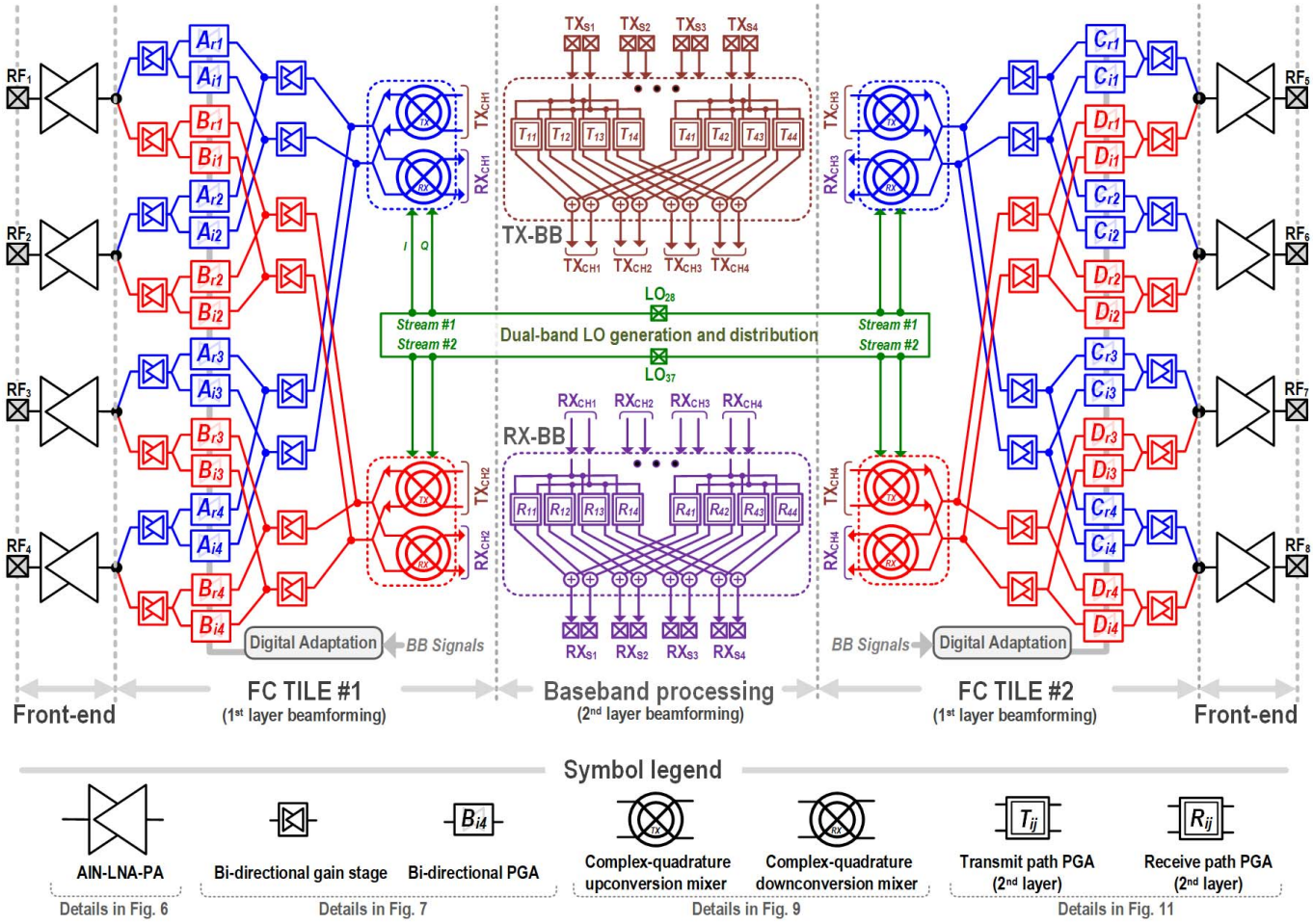


Fig. 5. Simplified schematic of two-layer eight-element four-stream HBF transceiver prototype.

The analog baseband weight layer is also designed to be FC, but the transmit and receive paths are not interleaved.

The Cartesian-combining/splitting technique described in Section III is used to perform RF-domain first-layer beamforming in each stream of the FC tile (the two streams in each tile are shown in red and blue in Fig. 5). In addition to its architectural advantages, the Cartesian-combining/splitting technique is well-suited to dual-band beamforming. This is because the RF-domain network is only based on programmable transconductors and current-mode combiners or voltage-mode splitters and can all be designed to have dual-band frequency responses. The frequency translation chains in each tile can select either 28- or 37-GHz LO, thereby providing maximum re-configurability between carrier-aggregation and MIMO modes. Compared to the heterodyne image-reject dual-band beamforming architecture described in [24], which minimizes the LO tuning range, the homodyne architecture used here is simpler and offers more flexibility in LO frequency selection and better cross-stream isolation at the expense of larger LO tuning requirements.

Our prototype transceiver comprises the following blocks: 1) one LNA/PA dual-band bidirectional interface per element shared between the two streams in each tile; 2) dual-band bidirectional beamforming network with shared passives between the TX and RX path for compactness; 3) one homodyne complex-quadrature up/down conversion stage per stream; 4) dual-band LO generation and distribution network; 5) baseband TX and RX second layer analog domain processing; and 6) digital control and adaptation circuitry. Design considerations of the key blocks are described next.

### A. LNA/PA and Bidirectional Antenna Interface Design

Each RF signal port of the chip connects to a dual-band, bidirectional front-end circuit that interfaces an antenna element to the first beamforming layer, as shown in Fig. 5. The front end, as shown in Fig. 6, comprises a low-noise amplifier, a power amplifier, and an antenna interface network, which combines a T/R switch function, a power combining function in transmit mode, and an input matching function in the receive mode. The front end is a refined version of the prototype [25]. As shown in [25], the FC first layer achieves better energy efficiency than a PC type when PAs with better back-off efficiency than Class-A are used. Therefore, the PAs in the present front end employ a two-way power combining topology with Class-B unit PAs in the output stage, each having a second-harmonic shorting network; this enables better peak and back-off efficiency. The front end can be

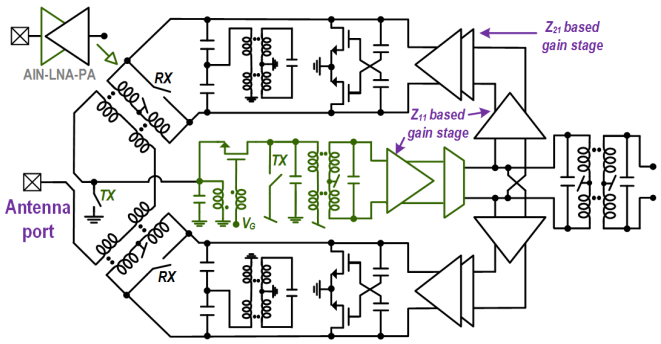


Fig. 6. Schematic of dual-band bidirectional front end consisting LNA, PA, and antenna interface switch.

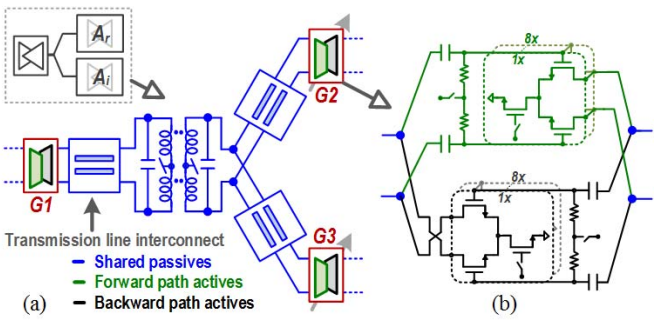


Fig. 7. Schematic of (a) reconfigurable bidirectional splitting/combining network and (b) programmable bidirectional transconductor.

switched between transmit and receive modes by means of three switches, as shown in Fig. 6 [25]. The output side series power combining network also constitutes an input matching network to the LNA, which uses a $G_m$-boosted common-gate input stage. All gain stages except the input LNA stage and the PA input stage use common-source differential pairs without a tail current source but with cross-coupled capacitive neutralization for improved differential mode stability. These stages use transformer coupled-resonator loads to obtain dual-band frequency responses. To equalize gains in the two bands, one gain stage in each of the LNA/PA paths uses driving port impedance ($Z_{11}$) load; all other stages use trans-impedance ($Z_{21}$) loads.

The antenna interface network design used in this prototype is compact and can operate concurrently in the two bands of interest. The interface switch avoids series quarter-wavelength transmission lines in the transmit and receive paths; such transmission lines are commonly used in front-end switches but occupy a large footprint and have high insertion loss [8]. In the switch designs in [7] and [8], the receive input experiences a tuned narrowband high impedance transmit-side load that limits the receiver's input match bandwidth. In contrast, in our interface network (see Fig. 6), the receive path input inductance can be reduced by turning ON the secondary side switch in the PA's output network. Thus, a fairly wideband input match can be achieved (measured $S_{11}$ around -12 dB/-8 dB for 28-/37-GHz bands). In the transmit mode, the loading from the OFF-state receive-side switch in [8] can reduce its bandwidth. Our simulations indicate that this can cause ~3-dB lower output power at 37 GHz when designed for the 28-GHz band [25]. In contrast, in the transmit mode for our interface network, the LNA input shorting switch reduces the PA's output power by only ~0.3 dB and does not cause bandwidth degradation. The isolation from the PA output to the LNA input is simulated to be 38/36 dB in the 28-/37-GHz band. The switch can configure the circuit between transmit and receive modes in a time on the order of a few nanoseconds; actual switching time is limited by the characteristics of the bias circuits and the power supply of the front end. An important refinement in the present transceiver's front end compared to our previous front-end design is that the gain of the LNA is increased by adding a gain stage using a $Z_{11}$-based load [25], [29]. This improves the overall LNA gain by 4 dB in the 28-GHz band and 11 dB in the 37-GHz band and results in a 26-dB gain in both bands. In the simulation, the receive path front end (in Fig. 6) achieves 5.3- and 6.5-dB NFs in 28- and 37-GHz bands, respectively. The transmit path achieves 26- and 28-dB gains, 14.5- and 15.5-dBm output referred 1-dB compression points ($oP_{1\,\mathrm{dB}}$), and 17.5% and 20% efficiencies at $oP_{1\,\mathrm{dB}}$ in simulation in 28- and 37-GHz bands, respectively.

### *B. RF Beamforming Layer Network*

The RF-domain beamforming network in the first layer is constructed by combining bidirectional sections similar to Fig. 7(a), following the system shown in Fig. 5. The section shown in Fig. 7(a) comprises three bidirectional transconductor stages ($G1$–$G3$) connected to a coupled resonator. Transconductors $G1$–$G3$ use cross-connected differential pairs, one of which is turned ON for forward or reverse signal flow (in the complex-weighting sections, these are binary-weighted, digitally switched [see Fig. 7(b)]). Thus, the signal path can be reversed without having switches in the RF signal path, thereby improving losses and bandwidth. Moreover, the cross-connected differential pairs [in Fig. 7(b)] also help improve differential mode stability of the entire combiner path by enabling self-neutralization through the gate-to-drain capacitance of the OFF-state path [25]. To improve common-mode stability, the center tap of the drive-side coil of each coupled-resonator in the beamforming network is connected to the power supply, while the center tap of the load-side coil is left open [25].

The secondary side of the coupled resonator serves as a voltage-splitter in receive mode (with $G1$–$G3$ in the forward mode) and a current-combiner load in transmit mode (with $G1$–$G3$ in the reverse mode). Using this structure in lieu of the traditional Wilkinson structure provides another advantage, namely, a third mode is available for current-mode SIC for simultaneous transmit–receive operation where $G1$ and $G2$ are set in the forward mode and $G3$ in the reverse mode. Passive structures throughout the first-layer network are shared between the TX and RX signal paths in order to reduce die area. The resulting compactness also helps minimize interconnect losses and, hence, overall power consumption. In the simulation, the entire beamforming path from an LNA's output to a downconverter input (an upconverter output to

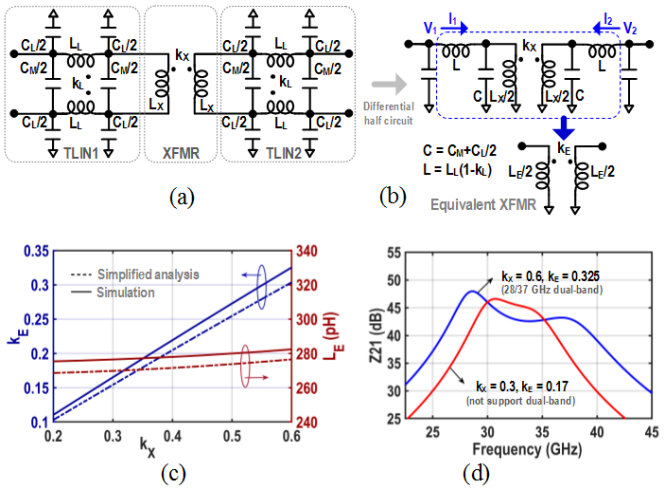


Fig. 8. Transmission line–transformer–transmission line system. (a) Simplified lumped element model. (b) Differential half circuit equivalent representation. (c) Effective coupling factor ($k_E$) and self-inductance ($L_E$) across transformer's coupling factor ($k_X$). (d) Transimpedance ($Z_{21}$) amplitude response for $k_X = 0.6$ and $k_X = 0.3$.

a PA input) achieves 4- and 0-dB (6- and 3-dB) gains in the 28- and 37-GHz bands, respectively.

### C. Front-End and First Layer Frequency Response

The front-end and first-layer beamforming network is designed to support concurrent operation in the 28- and 37-GHz bands. Their frequency responses are tailored by adjusting the coupling coefficient (and hence the poles) of the coupled resonators. A moderate coupling factor ($k_X = 0.25$–$0.35$) is chosen for the coupled-resonators in the LNA/PA stages, similar to in [24] and [25]. In the beamforming network, however, the presence of relatively long transmission lines (100–300 $\mu$m) between the active circuits and the coupled resonator loads leads to somewhat different design considerations, as discussed next. Specifically, it was found that a substantially higher coupling coefficient ($k_X = 0.4$–$0.6$) was required to achieve the requisite dual-band frequency response. Our design approach starts with analysis using lossless lumped-element models for the transmission line interconnect (parameters $L_L$, $k_L$, $C_L$, and $C_M$) and the transformer (parameters $L_X$ and $k_X$). The circuit is shown schematically in Fig. 8(a), and its differential-mode half-circuit equivalent is shown in Fig. 8(b). The voltages $V_1$ and $V_2$ and the currents $I_1$ and $I_2$ in Fig. 8(b) are related as follows:

$$V_1 = s[L + (L_X/2)(F_1/F_2)]I_1 + s[k_X(L_X/2)(1/F_2)]I_2$$
$$V_2 = s[k_X(L_X/2)(1/F_2)]I_1 + s[L + (L_X/2)(F_1/F_2)]I_2$$

where

$$F_1 = 1 - \omega^2(\mathrm{C}L_X/2) \times (1 - k_X^2)$$
$$F_2 = \left[1 - \omega^2(\mathrm{C}L_X/2)(1 + k_X)\right]\left[1 - \omega^2(\mathrm{C}L_X/2)(1 - k_X)\right]. \quad (4)$$

If we now represent the circuitry inside the blue dashed rectangle in Fig. 8(b) as an equivalent transformer with a coupling factor of $k_E$ and self-inductance of $L_E/2$, it can be derived from (4) that

$$L_E = 2L + L_X \times (F_1/F_2), k_E = k_X/(F_1 + F_2 \times 2L/L_X). \quad (5)$$

Therefore, in the presence of the transmission lines, the effective transformer coupling factor is reduced, and self-inductance is increased. Fig. 8(c) and (d) illustrates an exemplary scenario where two 240-$\mu$m transmission lines are symmetrically connected to a transformer ($L_X = 100$ pH and $k_X$ is tunable). The transmission line interconnect is first simulated using a field solver, and its lumped element parameters are extracted as $L_L = 155$ pH, $k_L = 0.52$, $C_M = 15$ fF, and $C_L = 40$ fF. It can be seen from Fig. 8(c) that the simulated $L_E$ and $k_E$ variations with $k_X$ closely match the simplified analysis in (5). As further verified in Fig. 8(d), the transimpedance of the composite transmission line and transformer system with moderate coupling coefficient ($k_X = 0.3$) has low bandwidth since the effective coupling coefficient is low ($k_E = 0.17$). On the other hand, the system can be made to operate as a dual-band load when a relatively high coupling factor $k_X = 0.6$ is chosen, which results in moderate effective coupling ($k_E = 0.325$).

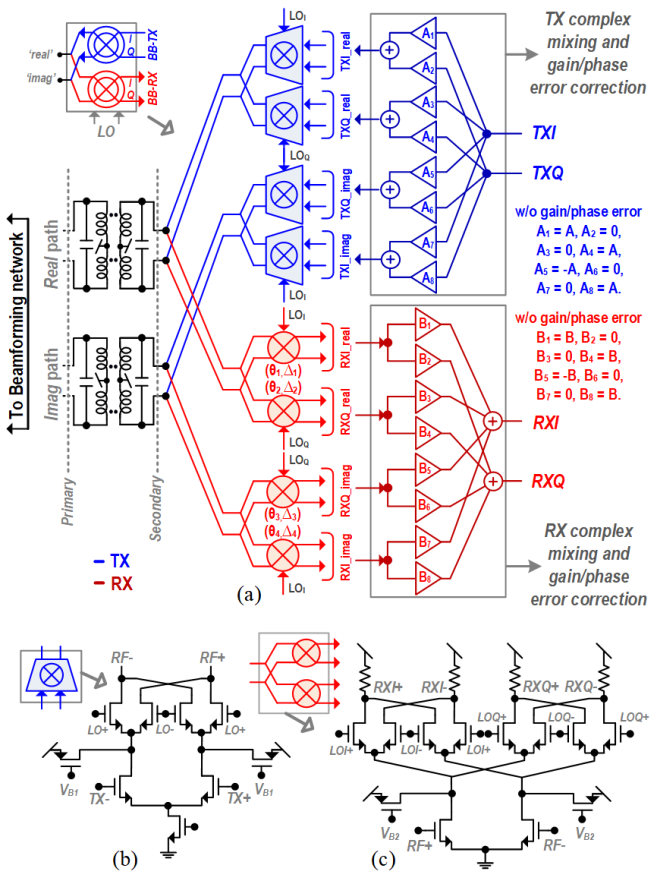


Fig. 9. (a) Bidirectional complex quadrature mixer. (b) Schematic of up-conversion mixing core w/o the load inductor. (c) Schematic of quadrature downconversion mixer.

### D. Frequency Translation Chain Design

Fig. 9 shows a detailed schematic of the bidirectional complex quadrature mixing stage. In each tile, the up- and

down-conversion mixing paths are connected to the beamforming network by a pair of coupled resonators (one each for the *real* and *imag* paths). The primary port of each coupled resonator connects to the bidirectional transconductors in the beamforming network. The secondary port of each coupled resonator acts as a load of a quadrature up-conversion stage and also as a splitting node to a quadrature downconversion stage.

The downconverted outputs of the quadrature mixer pairs in the receive path are weighted [$B_1$–$B_8$ in Fig. 9(a)] and summed to generate baseband quadrature outputs. The weights $B_1$–$B_8$ serve two purposes: first, to perform the output summing operation required to complete Cartesian-combining in the first beamforming layer; second, to correct for gain and phase errors. The nominal $B_1$–$B_8$ values in the absence of gain/phase errors are shown in Fig. 9(a). Including gain errors ($\Delta_1$–$\Delta_4$) and phase errors ($\theta_1$–$\theta_4$) of the four down-conversion mixing paths, the $B_1$–$B_8$ values are given as follows:

$$B_1 = \frac{\cos\theta_2}{\Delta_1 C_1}, \quad B_2 = \frac{-\sin\theta_2}{\Delta_1 C_1}, \quad B_3 = \frac{\sin\theta_1}{\Delta_2 C_1}, \quad B_4 = \frac{\cos\theta_1}{\Delta_2 C_1}$$
$$B_5 = \frac{-\cos\theta_4}{\Delta_3 C_2}, \quad B_6 = \frac{-\sin\theta_4}{\Delta_3 C_2}, \quad B_7 = \frac{-\sin\theta_3}{\Delta_4 C_2}, \quad B_8 = \frac{\cos\theta_3}{\Delta_4 C_2}$$

where

$$C_1 = \cos(\theta_1 - \theta_2) \quad \text{and} \quad C_2 = \cos(\theta_3 - \theta_4). \tag{6}$$

It should be noted that this scheme can correct for several types of gain/phase errors ($\theta_1$–$\theta_4$/$\Delta_1$–$\Delta_4$), including: 1) quadrature gain/phase error between I and Q LO paths; 2) gain/phase error within the two I paths or the two Q paths of the LO; and 3) gain/phase error between the *real* and *imag* signal paths.

Similar to the RX path, the $A_1$–$A_8$ weights in the TX path are applied to the baseband I/Q data streams to perform complex mixing and gain/phase error correction before being input to the upconversion mixers. The transistor-level schematic for the up-conversion mixing core (excluding the load transformer) and the quadrature down-conversion mixer are shown in Fig. 9(b) and (c), respectively. Current steering is used in both the up- and down-conversion mixing stages (using PMOS devices in Fig. 9(b) and (c), where the amount of current steering is set through $V_{B1}$ and $V_{B2}$) to improve linearity and noise performance. In the simulation, the down-conversion mixer achieves 6-dB conversion gain and 18-dB NF. The upconversion mixer achieves 6- and 1-dB conversion gains in the 28- and 37-GHz bands, respectively.

### *E. Dual-Band LO Generation and Distribution Network*

Since this transceiver employs direct conversion in both frequency bands, the LO distribution circuitry must have a frequency response that covers both bands. Moreover, since we desire the band for each stream (i.e., each up/downconversion pair) to be independently selectable, dedicated LO generation/distribution units are necessary for each stream. In this transceiver, LO synthesis circuitry is not included. However, it accepts single-ended LO signals in 28 and 37 GHz, from which differential-quadrature signals appropriate for feeding the active mixers shown in Fig. 9 are generated and distributed. The LO subsystem is shown in Fig. 10. The 28- and 37-GHz LO inputs are converted to the differential using baluns and then buffered and fed to coupled resonator quadrature hybrids (CRQHs), the design of which was described in detail in [30]. In contrast to other quadrature generation methods, the CRQHs are extremely compact, have low loss, and are easily implemented in differential form. The limited bandwidth over which the CRQH maintains a 90° phase difference is not an issue here because the CRQH can be tuned along with the LO frequency. In this transceiver, separate CRQHs are used for each band. The voltage outputs of the CRQHs are buffered by transconductors terminated in dual-band coupled resonator loads, as shown in Fig. 10. The LO fed to a particular stream is selected to either 28 or 37 GHz by switching ON or OFF the appropriate buffer transconductor. In the simulation, the LO path from the single-ended input to each of the I/Q differential output has 10- and 4-dB gains in the case of the 28- and 37-GHz paths, respectively.

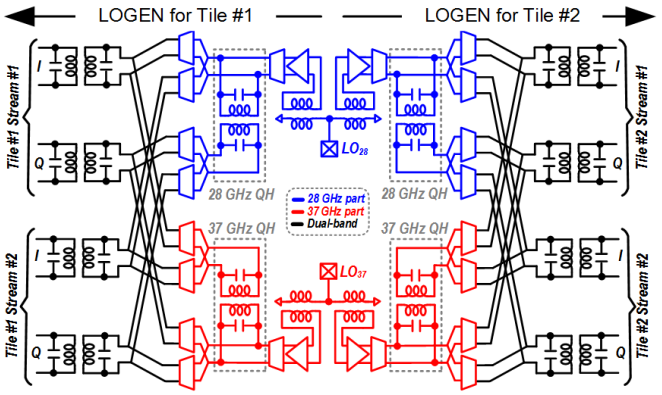


Fig. 10. Dual-band quadrature LO generation and distribution network for the two-tile four-stream MIMO HBF transceiver shown in Fig. 5.

### *F. Analog Baseband Beamforming Layer*

*1) Cartesian Baseband Beamforming:* The analog beamforming layer uses separate Cartesian complex-weights at baseband [2] for the transmit and receive paths (see Fig. 5). A detailed schematic of a section of the second beamforming layer is shown in Fig. 11(a), where Cartesian complex-weights are applied to two baseband streams and their outputs summed together, in accordance with the architecture of Fig. 5. Each complex-weight is realized using four programmable transconductors whose output currents are combined with appropriate polarity, as shown in Fig. 11(a). In-phase and quadrature components of output currents from two such complex-weights are summed together and converted to voltage using resistive loads (which use current bleeding to set the common-mode level). Each programmable transconductor has 6-bit (including sign bit) binary gain control, thereby enabling fine resolution baseband beamforming. A combination of binary and thermometer coding can be used to overcome non-monotonicity in the gain characteristic due to process variation and mismatch, but binary-only weighting was sufficient since $3\sigma$ gain variation was below $0.7\times$ LSB based on Monte Carlo simulation.

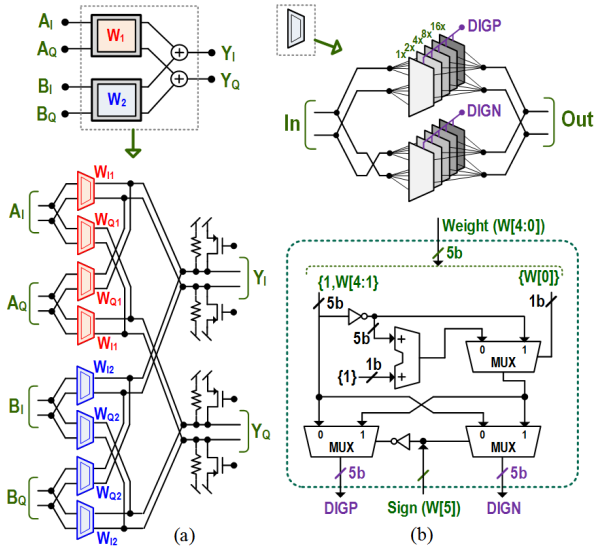


Fig. 11. (a) Baseband complex-weighting and combining. (b) Programmable sign-switchable transconductor that maintains the input and output impedance and quiescent current consumption across the tuning range.

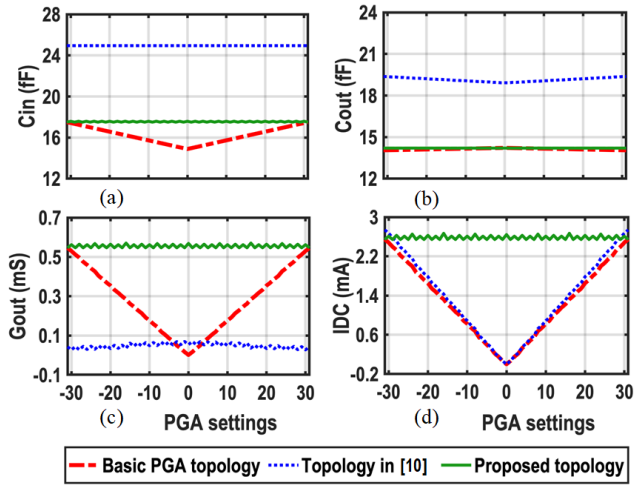


Fig. 12. Transconductors' performance across PGA settings for three different topologies—basic sign-switchable PGA, phase-invariant PGA in [10], and the PGA topology proposed in this work. (a) Input capacitance, (b) output capacitance, (c) output conductance, and (d) output node total DC current.

*2) New PGA Architecture:* An improved topology was sought for the programmable transconductor due to a large number of such cells and to achieve high complex-weighting accuracy over all possible settings. Desirable attributes of a programmable transconductor include precise linear increments, constant input and output capacitances and output resistance (to ensure phase invariance across settings), low hardware overhead, and constant output common-mode voltage. The phase-invariant topology described in [10] has the first two attributes. However, in order to present constant input capacitance, the design in [10] uses additional analog circuit blocks. Moreover, its common-mode voltage is a function of the gain setting. In order to overcome these limitations, the topology shown in Fig. 11(b) was developed, along with a digital encoding scheme that ensured constant capacitance, output resistance, and DC current.

The proposed transconductor is a binary-weighted array of cross-connected differential pairs. Each cell in the array can be turned ON or OFF by switching the bias of that cell's tail current source. A digital controller controls how the cells are turned ON or OFF, according to an algorithm discussed next. Suppose that the desired weight is represented as *W,* and the digital controls for the positive and negative polarity cells are *DIGP* and *DIGN*, respectively. Let the maximum value of *DIGP* or *DIGN* be $N$. The controller selects a set of values for *DIGP* or *DIGN* such that

$$DIGP - DIGN = W, \quad DIGP + DIGN = (N) \text{ or } (N+1). \quad (7)$$

That is, the total number of turned-ON cells is roughly constant (with an unavoidable one LSB variation) across the entire tuning range ($+N$ to $-N$). The solution to (7) can be shown to be the following:

$$DIGP = \lfloor (N+1+W)/2 \rfloor, \quad DIGN = \lfloor (N+1-W)/2 \rfloor. \quad (8)$$

Let us take two example cases with $W = 31$ and $W = -15$, where $N = 31$. According to (8), the *DIGP* and *DIGN* values for the first case are 31 and 0 and, for the second case, are 8 and 23, respectively. Based on the above design strategy, as the total turned-ON cells only vary by one LSB, the input capacitance, output impedance, and DC current variation are also bounded to one LSB variation between the ON and OFF unit cell. The digital control circuitry that implements the functionality in (8) is shown in Fig. 11(b).

The performance of the proposed transconductor (hereafter referred to as TOP#3) is compared next with two other topologies (TOP#1 and TOP#2). TOP#1 has the same topology as Fig. 11(b) but without the digital controller. In TOP#1, the top half is turned ON when $W > 0$ (i.e., $DIGP = W$ and $DIGN = 0$), and the bottom half is ON for $W < 0$ (i.e., $DIGP = 0$ and $DIGN = W$). TOP#2 is the design from [10] that uses separate constant capacitance and constant output impedance cells to ensure phase invariance. The following conclusions can be drawn from the comparison, whose results are plotted in Fig. 12.

1) TOP#2 and TOP#3 both have constant input capacitance. However, since TOP#3 does not require a dedicated capacitance compensation block, it has 30% lower input capacitance [see Fig. 12(a)].

2) TOP#2 and TOP#3 have constant output conductance [see Fig. 12(c)]. However, TOP#2 uses an explicit negative resistance cell whose bias current needs to be independently tuned and can also vary across the process. On the other hand, TOP#3 uses no additional analog hardware compared to TOP#1.

3) All three topologies have roughly constant output capacitance [see Fig. 12(b)]; however, TOP#2 has higher capacitance due to the use of the explicit conductance compensation cell.

4) TOP#3 consumes constant DC bias current [see Fig. 12(d)] across the tuning range, which helps keep the output common-mode voltage constant. Also, the DC power consumption of TOP#1 varies with weight setting, while the DC power consumption of TOP#3 (TOP#2) is constant

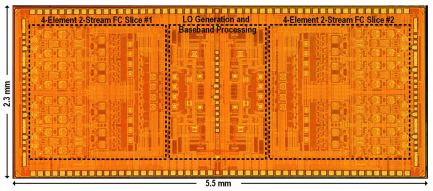


Fig. 13. Die micrograph of 28-/37-GHz two-layer HBF transceiver prototype.

and equals to (somewhat higher than) the maximum power consumption of TOP#1.

5) TOP#3 has a slightly higher die area than TOP#1 due to the digital controller, but TOP#2 consumes ∼40% more die area due to the additional analog blocks.

6) Unlike TOP#1 and TOP#2, where the input-referred noise power increases linearly for decreasing the weight settings from maximum, for TOP #3, it increases quadratically, and all designs have equal noise contribution for the full settings.

## V. Measurement Results

The dual-band two-layer eight-element HBF transceiver prototype is designed and fabricated in a 65-nm process (see Fig. 13) and consumes a 2.3 mm × 5.5 mm (12.65 mm$^2$) die area including pads. Each of the four-element two-stream RF FC-tile occupies 1.8 mm × 1.8 mm die area, including the bidirectional two-stream beamforming front-end and frequency translation stages. The LO generation and distribution network and the baseband beamforming layer occupy a total 1.89-mm$^2$ die area for eight elements together. This is equivalent to 0.81-mm$^2$ die area per element for two streams for bidirectional FC-tile and 1.05-mm$^2$ die area per element for two streams for the complete two-layer TRX beamforming. The ultra-compact Cartesian architecture, the custom-made mm-wave passive structures, and the sharing of passives between TX and RX modes help the prototype to achieve the lowest area consumption w.r.t. state-of-the-art single-layer beamforming transceivers even while supporting two MIMO streams (see Table I).

The eight-element two-layer MIMO prototype consumes a total of 1.37 A in the RX mode and 1.93 A in the TX mode from a 1-V power supply. The power breakdown is 8 × 26 mA in eight LNAs, 8 × 96 mA in eight PAs, 4 × 120 mA in the two-stream combiner in two tiles, 4 × 60 mA in the two up/down conversion mixers in two tiles, 2 × 122 mA in the LO generation in two tiles, and 2 × 100 mA in the TX/RX baseband layer in two tiles. This is equivalent to per element per-stream power consumption (calculated by dividing LNA/PA power by the number of elements only and other by the number of elements and streams) of 98.75 mW in the RX mode and 168.75 mW in the TX mode.

### A. Single-Element TX and RX Mode Characterization

A single element was first characterized in TX and RX modes with the *real/imag* path of one stream turned ON for one element (see Fig. 5) with full gain settings. The conversion gain is measured by sweeping the RF frequency and LO frequency together with a fixed IF of 50 MHz. The RF performance above (below) 33 GHz is measured using the 37-GHz (28-GHz) band LO path.

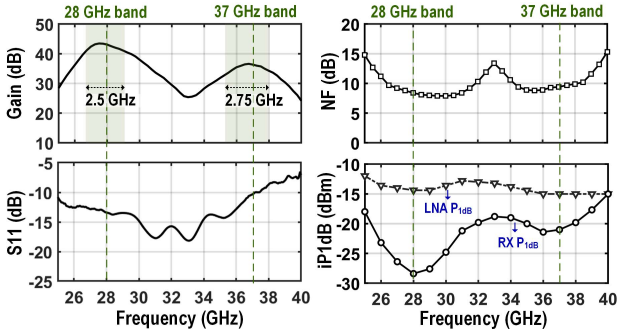


Fig. 14. Measured single-element receiver conversion gain, input return loss (S11), receiver noise figure, LNA input-referred $P_{1\,\mathrm{dB}}$, and receiver input-referred $P_{1\,\mathrm{dB}}$.

Fig. 14 shows single-element RX mode characterization results. The receiver achieves 44- and 37-dB peak conversion gains, 2.5- (26.5–29-GHz) and 2.75-GHz (35.25–38-GHz) RF bandwidths, 7.9- and 8.8-dB minimum noise figures, −12- and −8-dB $S_{11}$, and −29- and −22-dBm input-referred 1-dB compression points at 28- and 37-GHz bands, respectively. Next, the LNA linearity is measured by setting all blocks following the LNA at low gain settings to avoid any signal compression after the LNA. The LNA input-referred 1-dB compression point is −15 dBm in both bands (see Fig. 14). The wide RF bandwidth around each of the two concurrent bands enables the beamformer to support multiple channels in each band (up to ∼0.7 GHz of channel bandwidth can be supported in this design). Note that the dual-band frequency response helps filtering out unwanted spectral components in-between the two bands of interest. Although the front end supports two concurrent bands, the direct conversion architecture achieves high inter-band isolation through baseband filtering since the unwanted band appears at ∼9-GHz offset after the frequency translation.

Fig. 15(a) shows single-element TX mode characterization results. The transmitter achieves 43.5- and 40-dB peak conversion gains and 2.5- (27.2–29.7-GHz) and 2.75-GHz (35.05–37.8-GHz) RF bandwidths at 28- and 37-GHz bands, respectively. Next, the TX is characterized for large-signal performance. As shown in Fig. 15(b) and (c), the TX achieves 15.5- and 15.6-dBm peak output powers, 14- and 14.2-dBm output referred 1-dB compression points ($P_{1\,\mathrm{dB}}$), 21% and 21.5% peak PA efficiencies, and 15.5% and 17.2% PA efficiencies at $P_{1\,\mathrm{dB}}$ at 28- and 37-GHz bands, respectively. The PA large-signal performance across frequency is shown in Fig. 15(a).

The IF responses in TX and RX modes were measured in the 28- and 37-GHz bands. As shown in Fig. 16, in the RX path, ∼340-MHz 3-dB IF bandwidth is obtained in both bands, equivalent to 680-MHz two-sided RF bandwidth. Similarly, in the TX path, 260-MHz (520-MHz) IF bandwidth (two-sided RX bandwidth) is obtained.

On-chip fine-resolution baseband PGAs ($A_{1-8}$ and $B_{1-8}$ in Fig. 9) are adjusted in the measurement to improve TX

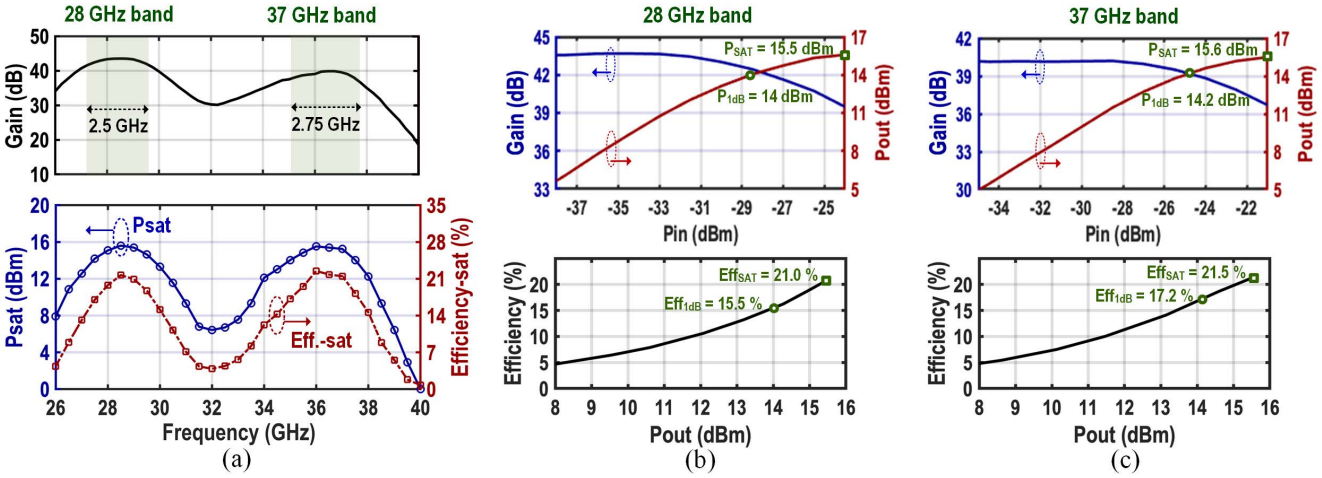


Fig. 15. (a) Measured single-element transmitter conversion gain, saturation output power ($P_{sat}$), and PA efficiency at $P_{sat}$ versus frequency. Large signal TX gain and output power versus input power, and PA efficiency versus output power in (b) 28- and (c) 37-GHz bands.

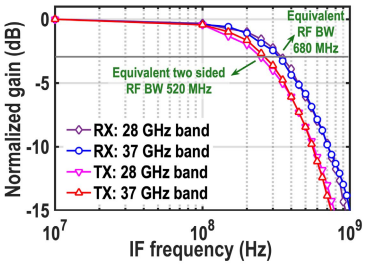


Fig. 16. TX and RX path IF bandwidth measurements.

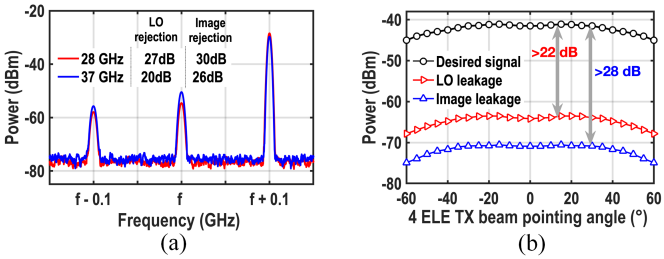


Fig. 17. (a) TX output signal spectrum in 28- and 37-GHz bands showing image-rejection and LO-rejection. (b) Image-rejection and LO-rejection toward the beam-pointing angle-of-departure for a four-element TX in the 28-GHz band across beam steering range of −60° to 60°.

and RX path image rejection and LO rejection. TX output spectrum for 28- and 37-GHz bands are shown in Fig. 17(a) with LO frequency set to 28 and 37 GHz, respectively, the IF frequency is set to +0.1 GHz and the TX output power is set at output referred P1dB. LO rejection of 27 dB (20 dB) and image rejection of 30 dB (26 dB) are achieved in the 28-GHz (37-GHz) band. In the case of a multi-antenna system, it is also important to achieve a good image and LO rejection when multiple elements are turned ON with different front-end phase settings. To this end, four TX elements are turned ON in measurement in the 28-GHz band with uniform linear array (ULA) of patch antennas (details of multi-antenna

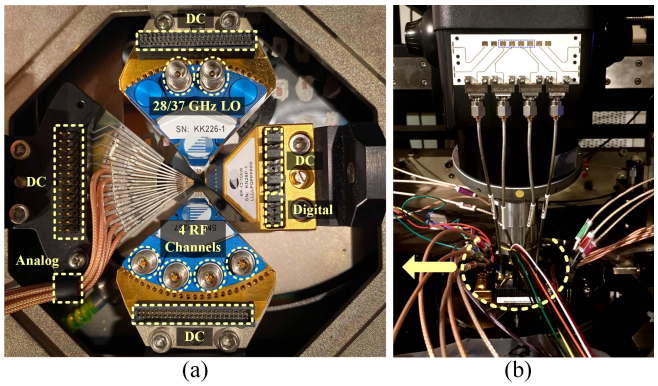


Fig. 18. (a) On-wafer probing setup with four probes simultaneously accessing 60 pads. (b) Setup photograph with four-element antenna array directly connected on the RF probe head for four-element OTA measurements.

measurement setup is elaborated in Section V-B), where weights are set to steer the beam across −60°–60° with a 5° step. Desired signal, an image signal, and LO leakage signal power are detected using a horn antenna RX at the other end of the link placed at the corresponding beam pointing direction. As shown in Fig. 17(b), over 22-dB LO rejection and over 28-dB image rejection are achieved across the beam steering range. On the other hand, in the RX mode, better than 1° and 0.3-dB I/Q phase and gain matching are achieved in both the 28-and 37-GHz bands, which translates to better than 35-dB image rejection. Note that both the image and LO rejection can further be improved by increasing baseband PGA resolution or by performing additional pre-/post-processing in the digital domain for the TX/RX path.

### *B. TX and RX Mode Beamforming*

Next, beam steering is characterized over-the-air (OTA) for a four-element array in the TX and RX modes using on-wafer probing. Fig. 18(a) shows the wafer probe setup that can access 4-RF input/output pads, two LO input pads, 12 analog/digital

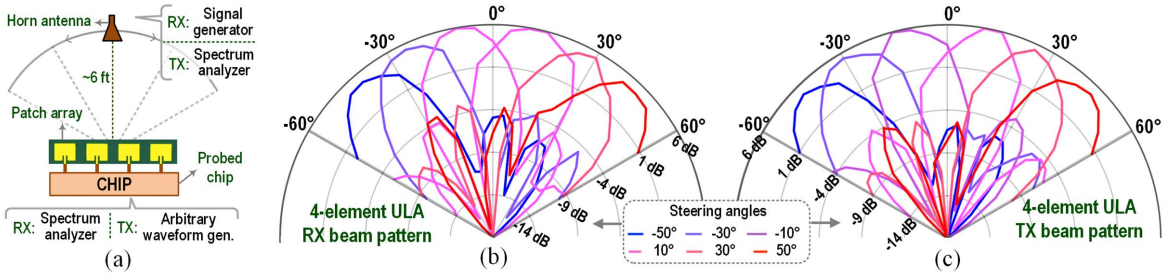


Fig. 19. (a) Measurement setup for beam pattern measurement using horn antenna and four-element patch antenna array. Measured four-element (b) RX and (c) TX beam patterns for six different beam steering angles.

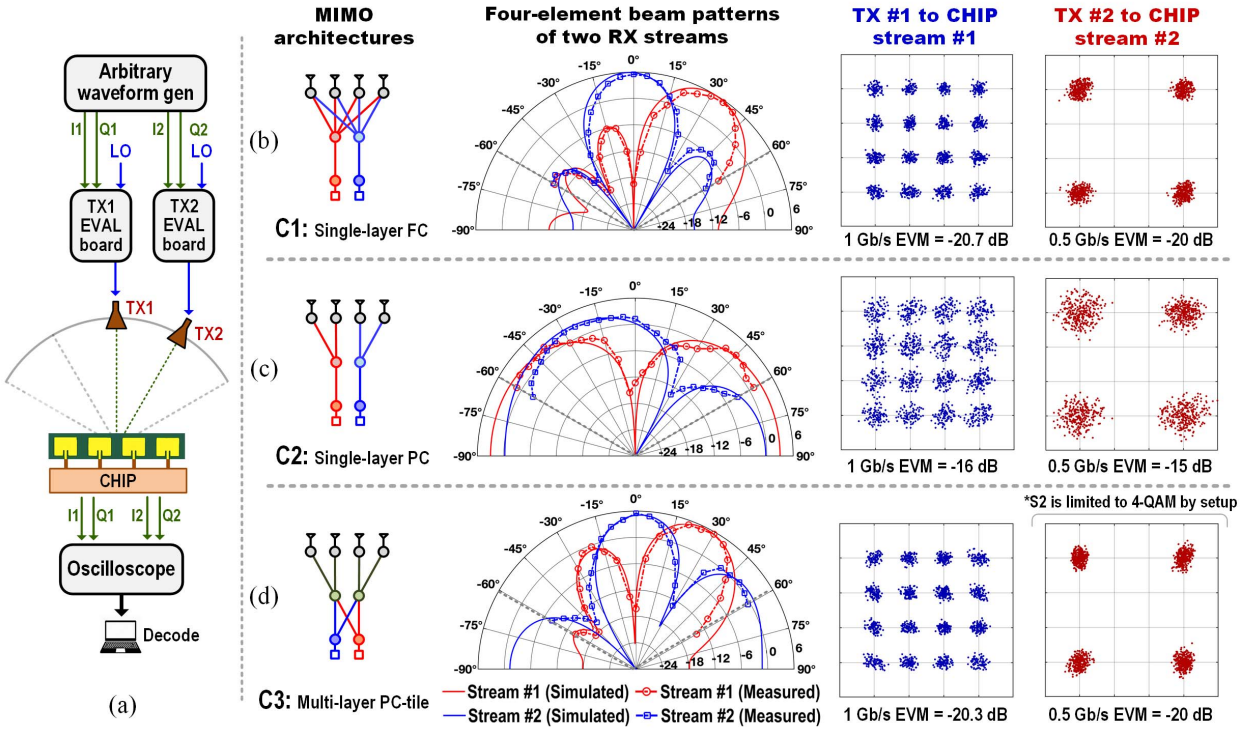


Fig. 20. (a) Two-stream simultaneous OTA MIMO measurement setup. Beam pattern measurement and modulated signal OTA measurement for concurrent two-stream spatial MIMO operation in case of (b) single-layer FC, (c) single-layer PC, and (d) two-layer architecture with PC-tile.

pads, and 42 power/ground pads. Measurements presented in Sections V-A–V-C were done using this setup. To conduct four-element OTA measurements with wafer probing, a ULA antenna was connected to an RF probe using short semi-rigid coaxial cables, as shown in Fig. 18(b). The patch array is designed to operate at a 28-GHz band with an element-to-element spacing of $\lambda/2$ at 28 GHz. A horn antenna is used at the opposite end of the link [see Fig. 19(a)]. In the RX mode, a continuous wave single tone RF signal is transmitted through the horn antenna OTA, which is then received by all four elements, downconverted to IF after beamforming, and observed through the spectrum analyzer. Similarly, in the TX mode, a continuous wave single-tone IF signal is applied to the chip, upconverted to RF, appropriately weighted to form a beam toward the angle of departure, and transmitted OTA, which is then received by the horn antenna and observed in the spectrum analyzer. The horn antenna is placed at a distance of ~6 ft and rotated with a 5° angular step along a semicircular path (keeping the patch array at the origin) while always pointing toward the patch array. A single-point angular calibration is performed at the 0° settings w.r.t. the normal of the patch array. At the 0° settings, complex-weights in each of the four elements are adjusted to receive/transmit synchronous signals, thereby calibrating out any mismatch between the four antenna-to-chip connections. The beam weights are pre-calculated based on the steering direction and applied to the chip through the SPI interface. The TX and RX mode beam patterns are shown in Fig. 19(b) and (c), respectively, for steering angles of −50°, −30°, −10°, 0°, 10°, 30°, and 50°. The measured beam patterns closely match the steering beam and null angles with better than 10-dB sidelobe performance (without tapering).

### C. Performance of Various Hybrid MIMO Architectures

Measurement setup for on-air four-element MIMO characterization is shown in Fig. 20(a). A four-element ULA is connected to the chip, and the chip is configured in two-stream RX mode to receive two independent data streams

simultaneously. On the TX side, two independent I/Q pairs of data streams are first generated using an arbitrary waveform generator (AWG), which is then upconverted to 28 GHz using two of-the-shelf up-conversion evaluation boards. The upconverted TX signals are then transmitted through two horn antennas that are placed at 0° and 30° relative to the normal of the RX array. Please note that our setup is limited to generating arbitrary modulation schemes only for one I/Q pair, and the other I/Q pair can only use the QPSK modulation scheme. On the RX side, the chip performs simultaneous beamforming, RF domain spatial filtering, and downconversion. Finally, the baseband RX (I/Q) outputs of both streams are simultaneously captured using an oscilloscope to analyze the received data (demodulation, synchronization, and plotting are done in MATLAB). No equalization and cross-stream rejection were applied in software or in the digital domain for the results in Fig. 20(b)–(d). Although the MIMO operation in HBF is partially verified with a two-element setup in our previous work, to the best of our knowledge, this is the first demonstration of the complete over the air simultaneous multi-user communication link measurement in the literature.

Here, the MIMO operation is characterized in three different configurations C1–C3 [see Fig. 20(b)–(d)]. In each configuration, beam weights are first computed based on the TX locations in order to steer beam toward the desired TX user while simultaneously steering null toward the undesired TX user. The computed weights are then applied to the chip using an SPI interface. In each configuration, the beam pattern is measured following the setup in Fig. 19(a) for each stream. The measured patterns [see Fig. 20(b)–(d)] match the simulations, and the two co-channel streams are decoded with high EVM in all configurations. The transmitted streams in this measurement have equal power, and the per-element per-stream average RX input power is set to approximately −60 dBm. The link is set up in a noise-limited state so that changes in EVM can be observed in Fig. 20(b)–(d) as the beamforming gain changes between the different configurations C1–C3. Fig. 20(b) shows that, in the case of a single-layer FC configuration in C1, simultaneous $10 \times \log(4) = 6$-dB beamforming gain can be achieved from four RX elements, thereby showcasing the advantage of an FC array. On the other hand, Fig. 20(c) shows that, in the case of a single-layer PC configuration in C2, simultaneous beamforming gain of only $10 \times \log(4/2) = 3$ dB can be achieved from four RX elements and two streams. However, Fig. 20(d) shows that, in the case of a two-layer PC configuration in C3, once we add the second layer of baseband processing, per-stream beamforming gain and EVM performance close to C1 can be achieved, thereby showcasing the effectiveness of two-layer MIMO processing. Therefore, measurements in Fig. 20(b)–(d) clearly show the tradeoff present in existing MIMO architectures and the benefit of the proposed architecture, as described in Section II.

### *D. Eight-Element TX and RX MIMO Characterization*

In order to exercise all eight elements and four RF chains, the chip is wire-bonded directly to a RO4003 PCB [see Fig. 21(a)]. The chip was placed inside a cavity in the PCB,

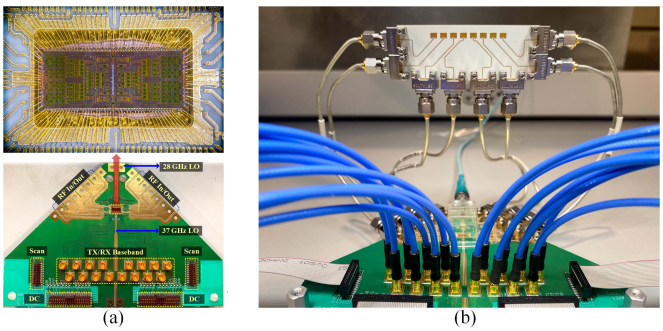


Fig. 21. (a) Chip-on-board PCB of the eight-element two-layer hybrid beamformer prototype. (b) Measurement setup consisting of the eight-element PCB connected to an eight-element ULA antenna array.

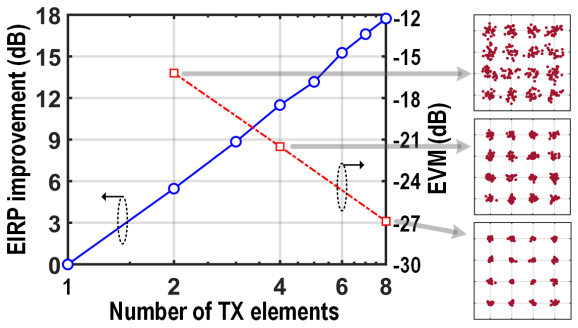


Fig. 22. EIRP improvement and EVM improvement across the number of turned-ON TX elements of the antenna array.

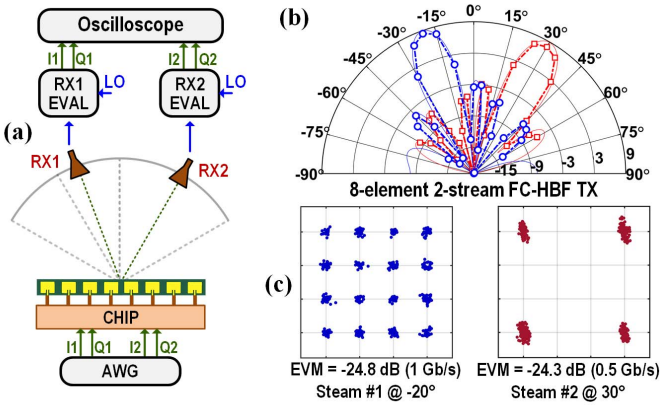


Fig. 23. (a) Eight-element two-stream simultaneous OTA TX MIMO measurement setup. (b) Beam pattern measurement and (c) modulated signal OTA measurement for concurrent two-stream spatial TX MIMO operation.

and care was taken to reduce bondwire length and loop height for the RF and LO signals. A photograph of a measurement setup of the eight-element prototype board connected to an eight-element ULA is shown in Fig. 21(b). This setup is used in the following eight-element OTA measurements.

First, eight-element transmit mode characterization is performed using a continuous-wave signal in the 28-GHz band. All eight elements are set to equal output power, and a horn antenna is used at the other end of the link to receive the spatially combined transmitted signals from the array. A single-point angular calibration, similar to the four-element case in

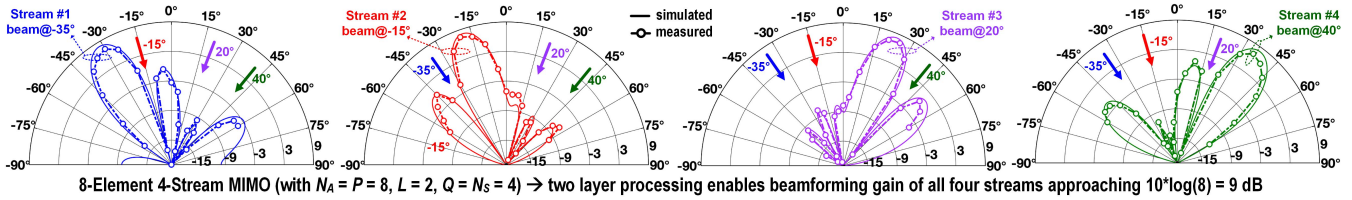


Fig. 24. Eight-element ULA four-stream MIMO measured beam patterns directing four simultaneous independent beams toward −35°, −15°, 20°, and 40°. Spatial null is directed toward undesired streams to achieve cross-stream isolation.

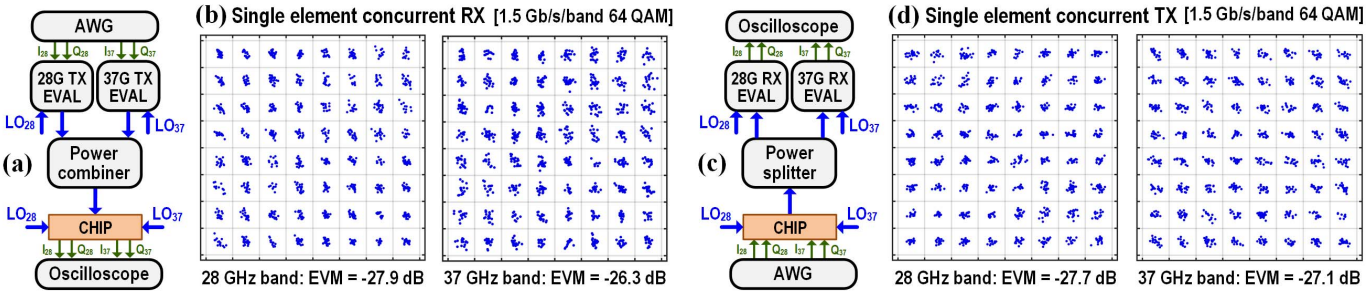


Fig. 25. Concurrent 28-/37-GHz single-element RX (a) measurement setup and (b) constellation measurements. Concurrent 28-/37-GHz single-element TX (c) measurement setup and (d) constellation measurements.

Section V-B, is performed at the 0° settings with respect to the normal of the patch array. At the 0° settings, complex-weights in the eight elements are adjusted to transmit synchronous signals. The horn antenna RX is placed at the 0° angular position. Fig. 22 shows the transmitted effective isotropically radiated power (EIRP) improvement with the number of turned-ON elements. As expected, the EIRP improvement is linear on a logarithmic scale, with approximately 6-dB EIRP improvement for every doubling of the transmit elements. Next, a modulated (1-Gb/s 16-QAM) single-stream signal is transmitted through the transmit array. The transmitted average output power per element is set to 0 dBm, and the link is set up in a noise-limited state to observe the change in EVM with improvement in EIRP for a fixed distance across the number of turned-ON elements. The other end of the link uses a 28-GHz downconverter. As can be seen from Fig. 22, EVM improvement of ∼6 dB is also observed with every doubling of the number of antennas. Note that the downconverter EVM is separately measured to be limited to −32 dB, which ensures that the downconverter linearity does not limit our EVM measurement.

Next, simultaneous two-stream transmit MIMO beamforming functionality is characterized with all eight elements using the setup shown in Fig. 23(a). The prototype chip is configured into two-stream FC mode to transmit two independent data streams simultaneously. Here, two four-element two-stream FC tiles together operate as an eight-element two-stream FC. On the TX side of the link, two independent data streams (I/Q) are generated using an AWG and applied to the prototype chip. Beam weights are set to direct two simultaneous TX beams toward −20° and 30° relative to the normal of the TX array. On the other side of the link, two horn antennas are placed at −20° and 30° angular positions [see Fig. 23(a)]. Each horn antenna output is down-converted using a 28-GHz down-conversion module, and the baseband RX (I/Q) outputs of both streams are simultaneously captured using an oscilloscope to analyze the received data. Here, the prototype chip performs simultaneous transmit beamforming and also creates spatial nulls using RF domain on-chip weighting to reduce leakage of one stream toward the angle of departure of the other. Fig. 23(c) represents raw measurements, i.e., no additional equalization or cross-stream rejection was applied in software. It can be seen from the beam pattern measurements in Fig. 23(b) that two independent beams are simultaneously formed at −20° and 30° angular directions with beamforming gain from both approaching 9 dB (maximum available from eight-antenna elements) and null depth better than 25 dB toward each other. Two independently modulated data streams are simultaneously transmitted next with per-element PA average output power for each stream set at around −12.5-dB back-off from the oP1dB to accommodate the modulation-dependent PAPR and the PAPR increase of 3 dB from two streams [25]. As can be seen from Fig. 23(c), two co-channel streams are decoded with high EVM (EVM can be further improved by improving cross-stream leakage with digital pre-processing).

Finally, simultaneous four-stream MIMO beamforming is characterized with all eight elements of the prototype chip connected to a ULA. It can be seen from Fig. 24 that successful four simultaneous beam steering is performed for an exemplary scenario of look angles −35°, −15°, 20°, and 40°. In addition to increasing $N_S$ to four, the two-layer processing in the FC tiles enables beamforming gain for all four beams approaching the maximum possible gain with eight antenna elements (i.e., 9 dB). In addition, over 25-dB null is steered toward the three undesired angles of arrivals for a particular stream, which enhances inter-stream isolation. It should be noted that the two-layer MIMO with FC tiles

TABLE I
COMPARISON WITH RECENT PHASED ARRAYS AND HYBRID BEAMFORMERS

| | This Work | | CMU ISSCC'19 | | Qualcomm ISSCC'18 | CMU ISSCC'18 | | IBM ISSCC'17 | LG RFIC'17 | UCSD RFIC'17 | CMU RFIC'17 |
|---|---|---|---|---|---|---|---|---|---|---|---|
| Technology | 65nm CMOS | | 65nm CMOS | | 28nm CMOS | 65nm CMOS | | 130nm SiGe | 28nm CMOS | 180nm SiGe | 65nm CMOS |
| Freq. (GHz) | 28 (2.5 GHz BW) | 37 (2.75 GHz BW) | 28 | 37 | 25-30.5 | 28 | 37 | 28 | 28 | 28-32 | 25-30 |
| RX Gain (dB) | 44 | 37 | 16.1[c] | 10.9[c] | 24 | 33 | 26.5 | 34 | 39 | 20[c] | 34 |
| $NF_{min}$ (dB) | 7.9 | 8.8 | 6.2[c] | 7.0[c] | 4.4 | 5.7 | 8.5 | 6[c] | 6.7 | 4.6[c] | 7.3 |
| S11 (dB) | -12 | -8 | -13.2 | -15.1 | <-10 | <-10 | <-15 | - | - | <-10 | <-8 |
| $P_{1dB}$ (dBm) | -29[a] (-15[b]) | -22[a] (-15[b]) | -15.7[c] | -14.5[c] | - | -30 | -23 | -22.5 | - | -22 | -29 |
| TX Gain (dB) | 43.5 | 40 | 28.5[c] | 26.2[c] | 34-44 | - | - | 24-32 | - | 14 | - |
| $P_{SAT}$ (dBm) | 15.5 | 15.6 | 15.8[c] | 16.8[c] | 14 | - | - | 16 | 10.5 | <13 | - |
| PA $Eff_{SAT}$ (%) | 21% | 21.5% | 20% | 21.6% | - | - | - | - | - | - | - |
| $P_{1dB}$ (dBm) | 14 | 14.2 | 14.1[c] | 15.2[c] | 12 | - | - | 13.5 | 9.5 | <11.7 | - |
| Power (mW)[d] | 98.75 (RX), 168.75 (TX-DC) | | 38[c](R),116[c](T) | | 42(R),90(T) | 52.5 (RX) | | 206(R),287(T) | 50(R),85(T) | 130[c](R),200[c](T) | 27.5(RX) |
| Area ($mm^2$)[d] | 1.05 | | 0.48[c] | | 1.16 | 0.46 | | 2.59 | 0.91 | 2.9[c] | 0.32 |
| Integration level | Full transceiver w/ mixer and LO distribution | | Single element front-end w/o mixer or LO | | Mixer, LO gen. and distribution | Mixer, LO distribution | | Mixer, LO distribution | Mixer, LO gen. and distribution | No mixer or LO | Mixer, LO distribution |
| Functionality | (1) Multi-layer MIMO w/ FC tile (2) FD beamforming w/ 3-step SIC | | MIMO-TDD/FD T/R Front-End | | T/R Phased Array | FC-HBF RX MIMO/CA | | T/R Phased Array | T/R Phased Array | T/R Phased Array | FC-HBF RX MIMO |

[a] full RX path, [b] LNA only, [c] Excluding up-/down-conversion, [d] Estimated for per-element per-stream,

also enables STAR operation along with MIMO, which will be demonstrated in our future publications.

### *E. Concurrent 28- and 37-GHz Band Operations*

Concurrent 28- and 37-GHz band performance is characterized next in transmit and receive modes for a single element. In the concurrent receive mode, two independently modulated data streams from two external up-converters (one at the 28-GHz band and the other at the 37-GHz band) are power combined and applied to one antenna element [see Fig. 25(a)]. One received stream is set to operate in the 28-GHz band and the other at the 37-GHz band to simultaneously down-convert both the incoming streams. The baseband received outputs from both streams are simultaneously collected through an oscilloscope. As shown in Fig. 25(b), for 1.5-Gb/s (64-QAM) data rate in each carrier independently, the RX EVM is −27.9 and −26.3 dB, respectively (peak received power is set as iP1dB of RX). Similarly, in the concurrent TX mode, two on-chip up-conversion paths of two streams operate: one in the 28-GHz band and the other in the 37-GHz band. Two upconverted data streams are combined on-chip at the input of the PA and are transmitted through one PA. The PA output is downconverted using two external down-converters operating one in each band [see Fig. 25(c)]. As shown in Fig. 25(d), for 1.5-Gb/s (64-QAM) data rate in each carrier, the TX EVM is −27.7 and −27.1 dB, respectively (peak TX power is set as oP1dB of TX). The above measurements demonstrate concurrent dual-band operation for a single element. Although the prototype can support concurrent carrier aggregation from multiple elements, the demonstration of multi-antenna carrier-aggregation requires designing a dual-band/wideband antenna array (a field of ongoing research [31]–[33]), which can be considered as future work.

## VI. CONCLUSION

This work makes two major contributions. First, a new two-layer hybrid MIMO architecture is introduced, which comprises multiple low-RF-complexity single-stream (PC) or multi-stream (FC) tiles in the first spatial-processing layer, followed by an FC analog/digital baseband second layer. This architecture mitigates the complexity versus spectral-efficiency tradeoffs between conventional single-layer PC and (our previously proposed) FC architectures and enables upward scaling of the number of MIMO streams. Second, an ultra-compact bidirectional reconfigurable dual-band two-layer beamforming circuit architecture is introduced, which includes various innovative circuit design techniques. While achieving state-of-the-art transceiver performance (see Table I), the eight-element four-stream dual-band prototype in this work demonstrates, for the first time, multi-user (up to four) OTA MIMO functionality using low-complexity highly energy-efficient FC RF-tiles with spectral-performance and flexibility approaching that of digital beamformers.

## REFERENCES

[1] K. Kibaroglu, M. Sayginer, and G. M. Rebeiz, "A low-cost scalable 32-element 28-GHz phased array transceiver for 5G communication links based on a 2 × 2 beamformer flip-chip unit cell," *IEEE J. Solid-State Circuits*, vol. 53, no. 5, pp. 1260–1274, Jan. 2018.

[2] S. Kundu and J. Paramesh, "A compact, supply-voltage scalable 45–66 GHz baseband-combining CMOS phased-array receiver," *IEEE J. Solid-State Circuits*, vol. 50, no. 2, pp. 527–542, Feb. 2015.

[3] S. Shahramian, M. J. Holyoak, A. Singh, and Y. Baeyens, "A fully integrated 384-element, 16-tile, W-band phased array with self-alignment and self-test," *IEEE J. Solid-State Circuits*, vol. 54, no. 9, pp. 2419–2434, Sep. 2019.

[4] Y. Yeh, B. Walker, E. Balboni, and B. Floyd, "A 28-GHz phased-array receiver front end with dual-vector distributed beamforming," *IEEE J. Solid-State Circuits*, vol. 52, no. 5, pp. 1230–1244, May 2017.

[5] T. Sowlatiet *et al.*, "A 60-GHz 144-element phased-array transceiver for backhaul application," *IEEE J. Solid-State Circuits*, vol. 53, no. 12, pp. 3640–3659, Dec. 2018.

[6] J. Pang *et al.*, "A 28-GHz CMOS phased-array transceiver based on LO phase-shifting architecture with gain invariant phase tuning for 5G new radio," *IEEE J. Solid-State Circuits*, vol. 54, no. 5, pp. 1228–1242, May 2019.

[7] J. D. Dunworth *et al.*, "A 28 GHz bulk-CMOS dual-polarization phased-array transceiver with 24 channels for 5G user and basestation equipment," in *IEEE Int. Solid-State Circuits Conf. (ISSCC) Dig. Tech. Papers*, vol. 61, Feb. 2018, pp. 70–72.

[8] B. Sadhu *et al.*, "A 28-GHz 32-element TRX phased-array IC with concurrent dual-polarized operation and orthogonal phase and gain control for 5G communications," *IEEE J. Solid-State Circuits*, vol. 52, no. 12, pp. 3373–3391, Dec. 2017.

[9] H. T. Kim *et al.*, "A 28-GHz CMOS direct conversion transceiver with packaged 2×4 antenna array for 5G cellular system," *IEEE J. Solid-State Circuits*, vol. 53, no. 5, pp. 1245–1259, May 2018.

[10] S. Mondal, R. Singh, A. I. Hussein, and J. Paramesh, "A 25–30 GHz fully-connected hybrid beamforming receiver for MIMO communication," *IEEE J. Solid-State Circuits*, vol. 53, no. 5, pp. 1275–1287, May 2018.

[11] A. Puglielli *et al.*, "Design of energy- and cost-efficient massive MIMO arrays," *Proc. IEEE*, vol. 104, no. 3, pp. 586–606, Mar. 2016.

[12] C. Fulton, M. Yeary, D. Thompson, J. Lake, and A. Mitchell, "Digital phased arrays: Challenges and opportunities," *Proc. IEEE*, vol. 104, no. 3, pp. 487–503, Mar. 2016.

[13] R. Garg *et al.*, "A 28-GHz beam-space MIMO RX with spatial filtering and frequency-division multiplexing-based single-wire IF interface," *IEEE J. Solid-State Circuits*, vol. 56, no. 8, pp. 2295–2307, Aug. 2020.

[14] S. Han, C.-L. I, Z. Xu, and C. Rowell, "Large-scale antenna systems with hybrid analog and digital beamforming for millimeter wave 5G," *IEEE Commun. Mag.*, vol. 53, no. 1, pp. 186–194, Jan. 2015.

[15] X. Gao, L. Dai, S. Han, I. Chih-Lin, and R. W. Heath, Jr., "Energy-efficient hybrid analog and digital precoding for mmWave MIMO systems with large antenna arrays," *IEEE J. Sel. Areas Commun.*, vol. 34, no. 4, pp. 998–1009, Apr. 2016.

[16] D. Zhang, Y. Wang, X. Li, and W. Xiang, "Hybridly connected structure for hybrid beamforming in mmWave massive MIMO systems," *IEEE Trans. Commun.*, vol. 66, no. 2, pp. 662–674, Feb. 2018.

[17] J. Du, W. Xu, H. Shen, X. Dong, and C. Zhao, "Hybrid precoding architecture for massive multiuser MIMO with dissipation: Sub-connected or fully connected structures?" *IEEE Trans. Wireless Commun.*, vol. 17, no. 8, pp. 5465–5479, Aug. 2018.

[18] M. Majidzadeh, A. Moilanen, N. Tervo, H. Pennanen, A. Tolli, and M. Latva-Aho, "Partially connected hybrid beamforming for large antenna arrays in multi-user MISO systems," in *Proc. IEEE 28th Annu. Int. Symp. Pers., Indoor, Mobile Radio Commun. (PIMRC)*, Oct. 2017, pp. 1–6.

[19] L. Dai, X. Gao, J. Quan, S. Han, and C.-L. I, "Near-optimal hybrid analog and digital precoding for downlink mmWave massive MIMO systems," in *Proc. IEEE Int. Conf. Commun. (ICC)*, Jun. 2015, pp. 1334–1339.

[20] X. Song, T. Kuhne, and G. Caire, "Fully-/partially-connected hybrid beamforming architectures for mmWave MU-MIMO," *IEEE Trans. Wireless Commun.*, vol. 19, no. 3, pp. 1754–1769, Mar. 2020.

[21] X. Zhu, Z. Wang, L. Dai, and Q. Wang, "Adaptive hybrid precoding for multiuser massive MIMO," *IEEE Commun. Lett.*, vol. 20, no. 4, pp. 776–779, Apr. 2016.

[22] X. Yu, J.-C. Shen, J. Zhang, and K. B. Letaief, "Alternating minimization algorithms for hybrid precoding in millimeter wave MIMO systems," *IEEE J. Sel. Topics Signal Process.*, vol. 10, no. 3, pp. 485–500, Apr. 2016.

[23] O. El Ayach, S. Rajagopal, S. Abu-Surra, Z. Pi, and R. W. Heath, Jr., "Spatially sparse precoding in millimeter wave MIMO systems," *IEEE Trans. Wireless Commun.*, vol. 13, no. 3, pp. 1499–1513, Mar. 2014.

[24] S. Mondal and J. Paramesh, "A reconfigurable 28-/37-GHz MMSE-adaptive hybrid-beamforming receiver for carrier aggregation and multi-standard MIMO communication," *IEEE J. Solid-State Circuits*, vol. 54, no. 5, pp. 1391–1406, May 2019.

[25] S. Mondal and J. Paramesh, "Power-efficient design techniques for mm-wave hybrid/digital FDD/full-duplex MIMO transceivers," *IEEE J. Solid-State Circuits*, vol. 55, no. 8, pp. 2011–2026, Aug. 2020.

[26] A. F. Molisch *et al.*, "Hybrid beamforming for massive MIMO: A survey," *IEEE Commun. Mag.*, vol. 55, no. 9, pp. 134–141, Sep. 2017.

[27] S. Mondal, L. R. Carley, and J. Paramesh, "A 28/37 GHz scalable, reconfigurable multi-layer hybrid/digital MIMO transceiver for TDD/FDD and full-duplex communication," in *IEEE Int. Solid-State Circuits Conf. (ISSCC) Dig. Tech. Papers*, Feb. 2020, pp. 82–84.

[28] J. Paramesh, R. Bishop, K. Soumyanath, and D. J. Allstot, "A four-antenna receiver in 90-nm CMOS for beamforming and spatial diversity," *IEEE J. Solid-State Circuits*, vol. 40, no. 12, pp. 2515–2524, Dec. 2005.

[29] R. Singh, S. Mondal, and J. Paramesh, "A millimeter-wave receiver using a wideband low-noise amplifier with one-port coupled resonator loads," *IEEE Trans. Microw. Theory Techn.*, vol. 68, no. 9, pp. 3794–3803, Sep. 2020.

[30] R. Singh, S. Mondal, and J. Paramesh, "A compact digitally-assisted merged LNA vector modulator using coupled resonators for integrated beamforming transceivers," *IEEE Trans. Microw. Theory Techn.*, vol. 67, no. 7, pp. 2555–2568, Jul. 2019.

[31] S. Lee, S. Kim, and J. Choi, "Dual-band dual-polarized proximity fed patch antenna for 28 GHz/39 GHz 5G millimeter-wave communications," in *Proc. 13th Eur. Conf. Antennas Propag. (EuCAP)*, 2019, pp. 1–5.

[32] Y. He, M. Rao, Y. Liu, G. Jing, M. Xi, and L. Zhao, "Millimeter wave stacked patch antenna array for 5G applications," in *Proc. Int. Work. Antenna Technol.*, 2020, pp. 5–8.

[33] H. M. Marzouk, M. I. Ahmed, and A.-E.-H. Shaalan, "Novel dual-band 28/38 GHz MIMO antennas for 5G mobile applications," *Prog. Electromagn. Res. C*, vol. 93, pp. 103–117, Mar. 2019.


**Susnata Mondal** (Member, IEEE) received the B.Tech. and M.Tech. degrees (integrated five-year program) in electronics engineering from IIT Kharagpur, Kharagpur, India, in 2015, and the Ph.D. degree in electrical and computer engineering from Carnegie Mellon University, Pittsburgh, PA, USA, in 2020.

In 2013, he was a Research Intern with RWTH Aachen University, Aachen, Germany. Since 2020, he has been a Research Scientist with Intel Labs, Hillsboro, OR, USA, where he works on high-speed electrical/optical transceivers. His current research interests include millimeter-wave circuit design, algorithm and system design for multi-antenna wireless, and RF/mixed-signal design for high-speed wireline/optical links.

Dr. Mondal was a recipient of the DAAD WISE Fellowship in 2013, the Best B-Tech Project Award at IIT Kharagpur in 2014, the Analog Devices Outstanding Student Designer Award in 2017, the IEEE Solid-State Circuits Society Predoctoral Achievement Award in 2019, and the A.G. Milnes Award (Best Ph.D. Thesis Award) from Carnegie Mellon University in 2021. He was selected as the Solid-State Circuits Society (SSCS) Rising-Star in ISSCC 2020.

**Larry Richard Carley** (Life Fellow, IEEE) received the B.S., M.S., and Ph.D. degrees from the Massachusetts Institute of Technology, Cambridge, MA, USA, in 1976, 1978, and 1984, respectively.

He joined Carnegie Mellon University (CMU), Pittsburgh, PA, USA, in 1984. In 2001, he was appointed as the STMicroelectronics Professor of engineering at CMU. He has authored 28 patents. He has authored or coauthored over 200 technical articles and over 20 books and/or book chapters. His current research interests include analog and RF integrated circuit design in deeply scaled CMOS technologies and novel nanoelectromechanical device design and fabrication.

Dr. Carley was a recipient of numerous awards, including the Best Technical Paper Awards at both the 1987 and the 2002 Design Automation Conferences.

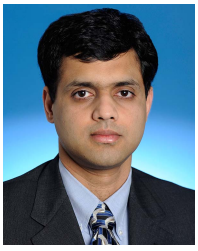

**Jeyanandh Paramesh** (Senior Member, IEEE) received the B.Tech. degree in electrical engineering from IIT Madras, Chennai, India, the M.S. degree in electrical engineering from Oregon State University, Corvallis, OR, USA, and the Ph.D. degree in electrical engineering from the University of Washington, Seattle, WA, USA.

He has held product development and research positions at AKM Semiconductor (Analog Devices), Motorola, and Intel. He is currently with SpaceX and holds an adjunct professorship at the Department of Electrical and Computer Engineering, Carnegie Mellon University, Pittsburgh, PA, USA. His current research interests include the design of RF and mixed-signal integrated circuits and systems for a wide variety of applications.